

Controls on spatial and temporal patterns of slope deformation in a paraglacial environment

Nicolas Oestreicher¹, Simon Loew², Clément Roques³, Jordan Balfour Aaron¹, Adriano Gualandi⁴, Laurent Longuevergne⁵, Philippe Limpach⁶, and Marc Hugentobler¹

¹ETH Zurich

²Swiss Federal Institute of Technology in Zurich

³University of Rennes 1

⁴Istituto Nazionale di Geofisica e Vulcanologia

⁵CNRS - Université Rennes 1

⁶Terradata

November 21, 2022

Abstract

A comprehensive surface displacement monitoring system installed in the recently deglaciated bedrock slopes of the Aletsch Valley shows systematic reversible motions at the annual scale. We explore potential drivers for this deformation signal and demonstrate that the main driver is pore pressure changes of phreatic groundwater in fractured granitic mountain slopes. The spatial pattern of these reversible annual deformations shows similar magnitudes and orientations for adjacent monitoring points, leading to the hypothesis that the annually reversible deformation is caused by slope-scale groundwater elevation changes and rock mass properties. Conversely, we show that the ground reaction to infiltration from snowmelt and summer rainstorms can be highly heterogeneous at local scale, and that brittle-ductile fault zones are key features for the groundwater pressure-related rock mass deformations. We also observe irreversible long-term trends (over the 6.5 yr dataset) of deformation in the Aletsch valley composed of a larger uplift than observed at our reference GNSS station in the Rhone valley, and horizontal displacements of the slopes towards the valley. These observations can be attributed respectively to the elastic bedrock rebound in response to current glacier mass downwasting of the Great Aletsch Glacier and gravitational slope deformations enabled by cyclic groundwater pressure-related rock mass fatigue in the fractured rock slopes.

Abstract

19 A comprehensive surface displacement monitoring system installed in the recently deglaciated
20 bedrock slopes of the Aletsch Valley shows systematic reversible motions at the annual
21 scale. We explore potential drivers for this deformation signal and demonstrate that the
22 main driver is pore pressure changes of phreatic groundwater in fractured granitic moun-
23 tain slopes. The spatial pattern of these reversible annual deformations shows similar
24 magnitudes and orientations for adjacent monitoring points, leading to the hypothesis
25 that the annually reversible deformation is caused by slope-scale groundwater elevation
26 changes and rock mass properties. Conversely, we show that the ground reaction to in-
27 filtration from snowmelt and summer rainstorms can be highly heterogeneous at local
28 scale, and that brittle-ductile fault zones are key features for the groundwater pressure-
29 related rock mass deformations. We also observe irreversible long-term trends (over the
30 6.5 yr dataset) of deformation in the Aletsch valley composed of a larger uplift than ob-
31 served at our reference GNSS station in the Rhone valley, and horizontal displacements
32 of the slopes towards the valley. These observations can be attributed respectively to the
33 elastic bedrock rebound in response to current glacier mass downwasting of the Great
34 Aletsch Glacier and gravitational slope deformations enabled by cyclic groundwater pressure-
35 related rock mass fatigue in the fractured rock slopes.
36

Plain Language Summary

37 Mountain ranges are subject to deformation due to tectonic forces, orogenesis, ero-
38 sion, and gravity. Other factors can deform the slopes, such as atmospheric-driven ther-
39 mal expansion and contraction, freeze-thaw in open fractures, and pore pressure vari-
40 ations. Close to retreating glaciers, the mechanical unloading of the ice body, and rapidly
41 changing thermal and hydrologic conditions lead to deformation of the slopes. The dif-
42 ficulty resides in identifying the different factors contributing to the total deformation.
43 We track surface displacements of fractured crystalline rock slopes adjacent to the Great
44 Aletsch Glacier (Switzerland) tongue for more than six years at unprecedentedly high
45 spatial and temporal resolutions. Our results demonstrate that groundwater is a crit-
46 ical driver of deformation. Centimetric reversible outward displacements are observed
47 after the snowmelt season each year, followed by a seasonal recession to which are su-
48 perimposed displacements caused by heavy rainfall-recharge events. Fault zones can be
49 key features where most of the hydromechanical deformation occurs, and their geome-
50

51 try can control the direction of deformation. Glacier melting induces long-term trends
52 of deformation. In addition, annual pore-pressure cycles lead to hydromechanical fatigue
53 processes. This work opens a new vision on the spatial and temporal variability of pro-
54 cesses responsible for bedrock deformation in paraglacial mountain slopes.

55 **1 Introduction**

56 Mountain slopes in paraglacial environments are perturbed when glaciers retreat.
57 These perturbations induce surface displacements in adjacent slopes, which can be re-
58 lated to subsurface damage from fracture propagation (e.g., Grämiger et al., 2018, 2020)
59 potentially leading to slope destabilization and collapse (e.g., Gischig et al., 2011; Loew
60 et al., 2017). In addition to unloading due to glacier ice downwasting (e.g., Mey et al.,
61 2016; Leith et al., 2014), seasonal deformation in response to temperature fluctuations
62 (e.g., Weber et al., 2019; Hugentobler et al., 2020), snow load (e.g., Heki, 2001) and pore-
63 pressure variations (e.g., Silverii et al., 2020) might contribute to long-term rock mass
64 fatigue and progressive failure (Eberhardt et al., 2004; McColl, 2012).

65 Many authors have analysed cyclic displacements in rock slopes with horizontal and
66 vertical peak-to-peak amplitudes up to 5 cm and 4 cm respectively (e.g., Loew et al., 2007;
67 Oestreicher, 2018; Silverii et al., 2020; Grämiger et al., 2020). Yet, the contribution of
68 the different factors in driving spatial and temporal variability in deformation remains
69 poorly understood due to the limited access to long-term, high-resolution (both spatial
70 and temporal) datasets. This paper describes and interprets one such dataset in order
71 to understand drivers of slope displacements in a paraglacial environment.

72 Cyclic rock slope deformations have been explained using a variety of short-term
73 environmental drivers (Tsai, 2011). Seasonal temperature differences cause thermoelas-
74 tic deformation of near-surface rocks (Prawirodirdjo et al., 2006; Tsai, 2011) which were
75 observed at various places in mountain bedrock around the world (Gischig et al., 2011;
76 Weber et al., 2017; Collins & Stock, 2016; Collins et al., 2018; Marmoni et al., 2020). Some
77 of these studies report rock mass strains amounting to 500 $\mu\text{m}/\text{m}$ for daily and seasonal
78 temperature variations (Marmoni et al., 2020) and up to centimetric aperture variations
79 of cracks in specific conditions (Collins & Stock, 2016; Collins et al., 2018). In gneisses
80 and granites of the Swiss Alps, the maximum peak-to-peak amplitude of single crack de-

81 formation was measured with crack extensometers between 2 mm (Gischig et al., 2011)
82 and 4 mm (Weber et al., 2017).

83 In alpine regions, frost-heave by ice segregation can induce large deformation of the
84 ground if open fractures close to the surface are filled with water and exposed to freez-
85 ing temperatures (Gruber & Haeberli, 2007; Matsuoka, 2008; Girard et al., 2013). In ad-
86 dition, the phase change of the water from liquid to solid implies a volume change of around
87 9 % (Lundberg et al., 2016), which can increase the stress normal to the fracture walls
88 and induce additional opening of fractures (Matsuoka, 2008; Musso Piantelli et al., 2020).
89 Wegmann and Gudmundsson (1999) observed deformation in gneissic rock walls of the
90 Aar massif explained by frost heave, and Matsuoka (2008) also described rainfall-related
91 frost during spring and autumn, with freezing temperatures overnight.

92 Loading and unloading of the surface, often associated with hydrologic cycles, can
93 induce cyclic displacements at continental scale (Van Dam et al., 2001) as well as the
94 regional to local scale (Heki, 2001; Moreira et al., 2016). In mountainous regions, this
95 process has been studied in both the Himalayan region (Bettinelli et al., 2008; Flouzat
96 et al., 2009; Chanard et al., 2014; Gautam et al., 2017; Gahalaut et al., 2017), the South-
97 ern European Alps (Serpelloni et al., 2018; Pintori et al., 2021) and the Apennines (Silverii
98 et al., 2019). In the Himalayan region, the peak-to-peak amplitude of the annual cyclic
99 deformation of cGPS stations was measured up to 23.8 mm horizontally and 14.8 mm ver-
100 tically at a cGPS station (Flouzat et al., 2009). The snow load in the mountains of north-
101 ern Japan induces peak-to-peak deformation between mid-march and mid-august at cGPS
102 stations up to around 17 mm vertically and around 5 mm horizontally (Heki, 2001). Ad-
103 ditionally, Drouin et al. (2016) showed that surface loading by snow accumulation in win-
104 ter is sufficient to produce measurable ground deformation in Iceland.

105 At depth, pore-pressure variations linked to groundwater table changes can induce
106 a poroelastic response of the rock mass, e.g. Wang (2000), after Biot (1941) and Rice
107 and Cleary (1976). Hansmann et al. (2012) found that the annual groundwater table vari-
108 ations could explain the deformation observed in granitic rocks of the Gotthard massif.
109 Valley perpendicular deformations, measured with robotic total positioning stations (TPS),
110 were found to have amplitudes as high as 6 mm (as the TPS measured cumulative dis-
111 placements from both sides of the valley, we report half of the annual amplitude of the
112 signal). In the Southern European Alps and the Apennines, several studies hypothesize

113 that pore pressure variations can explain the deformation of the region (e.g., Grillo et
114 al., 2018; Serpelloni et al., 2018; Braitenberg et al., 2019; Pintori et al., 2021). Such de-
115 formation is mainly highlighted in karstic systems, where large variations of water level
116 result in large localized deformation following heavy rainfall events (Braitenberg et al.,
117 2019).

118 Over longer timescales, multiple environmental and tectonic factors drive moun-
119 tain slope deformations in paraglacial environments (e.g. mass displacement in the as-
120 thenosphere, crustal tectonics, unloading by erosion, viscous, plastic, or elastic effects
121 of deglaciation). These slow (decades to millions of years) changes are recorded as long-
122 term trends in deformation time series. When interpreting these trends, the mixing of
123 signals from various sources often makes it challenging to identify the most important
124 causal factors (e.g., Sternai et al., 2019, and references therein). For the central Alps,
125 Sternai et al. (2019) propose that around 70 % of the measured uplift is caused by deglacia-
126 tion (viscous isostatic rebound of the last glacial maximum (LGM) and elastic rebound
127 from current ice loss), and around 30 % could be caused by deep mass movements in the
128 asthenosphere. At the scale of a single valley, deglaciation can have multiple effects. Dur-
129 ing the ice retreat, elastic uplift of the ground has been observed using GNSS stations
130 around large ice caps (e.g., Jiang et al., 2010; Ludwigsen et al., 2020). Further, in alpine
131 valleys, the topography results in spatial variations of ice elevation, potentially induc-
132 ing differential uplift (Ustaszewski et al., 2008). Grämiger et al. (2017) modeled the de-
133 formation response of a valley to the ice retreat from the LGM and showed that, in ad-
134 dition to differential uplift increasing towards the center of the valley, horizontal displace-
135 ment of the valley flanks is expected. The motion is rotational, directed away from the
136 valley center for the top parts of the slopes and towards it for the lower part (Grämiger
137 et al., 2017, figure 16). Accounting for thermomechanical effects during deglaciation, Grämiger
138 et al. (2018) show that there is an increase in damage compared to a purely mechani-
139 cal model and Grämiger et al. (2020) show a further increase in damage related to hy-
140 dromechanical effects. An important observation from Grämiger et al. (2020) is that by
141 changing the groundwater table in the slopes together with the change in ice elevation
142 in their model, the top part of the slope also moves towards the center of the valley dur-
143 ing deglaciation, contrarily to the purely mechanical model.

144 While all of the aforementioned processes can induce reversible surface deforma-
145 tions, it is often difficult to determine which process is dominant in alpine paraglacial

146 environments. Separating the different sources requires high-resolution deformation mon-
147 itoring, both temporal and spatial, and monitoring other environmental parameters such
148 as climate, hydrology and groundwater. So far, detailed studies of slope deformation fol-
149 lowing deglaciation have mainly focused on reactivation of slope instabilities (e.g. Glueer
150 et al., 2020) or on deformation of sediment slopes (Cody et al., 2020). A study of bedrock
151 deformation following deglaciation at the valley scale is missing.

152 The aim of this study is to assess the relative importance of various contributing
153 factors to time-dependent surface deformation in alpine paraglacial environments, includ-
154 ing near-surface air temperature, surface loads (e.g. ice, snow), and pore-pressure changes
155 in the subsurface. We test the following hypotheses:

- 156 1. that the strongest reversible slope deformations are caused by hydromechanically
157 coupled deformations driven by seasonal groundwater recharge and discharge cy-
158 cle,
- 159 2. that hydromechanically coupled deformations may have an irreversible component,
160 which can be used to evaluate rockmass damage.

161 In addition we will explore the spatial patterns of reversible and irreversible deforma-
162 tions in an alpine paraglacial catchment and relate them to the underlying mechanisms
163 and geological and hydrological factors controlling this spatial variability at regional and
164 local scales.

165 **2 Study site around the tongue of the Great Aletsch glacier and in-** 166 **stalled instrumentation**

167 Our study area is located in the central Swiss Alps, in the upper Valais, in a val-
168 ley oriented SW-NE, roughly parallel to the adjacent Rhone valley (situated ~ 5 km to
169 the SW), but with a higher (~ 800 m) elevation of the valley bottom. The bedrock is formed
170 of Paleozoic medium to high-grade metamorphic rocks (Schaltegger, 1994), and intru-
171 sions of central Aar granite, together with various types of dykes (Steck, 1983). These
172 rocks underwent the Alpine ductile and brittle deformations and subsequent formation
173 of a penetrative SW-NE striking Alpine foliation dipping steeply to the SE (Steck, 1983).
174 The valley is occupied by the Great Aletsch Glacier (see Figure 1). Deposits of glacial
175 till on bedrock in the study area can be related to three main stages: higher elevation
176 (2100-2300 masl), well-vegetated Egesen moraines, lower elevation (1900-2100 masl) and

177 less vegetated LIA moraines, and recent, usually relatively thin till deposits from the cur-
178 rent glacier retreat. The latter are sparsely vegetated. The area monitored for surface
179 deformation covers 12.8 km², of which 9 % is ice-covered, 26 % is covered by moraines and
180 debris and 65 % is partly exposed bedrock.

181 Numerous slope instabilities have been mapped and analyzed in the valley (Glueer
182 et al., 2019). The active Driest and Moosfluh landslides (see Figure 2) are situated around
183 the current position of the glacier tongue and show displacements of a few millimeters
184 per year up to meters per day for part of the Moosfluh landslide in September 2016 (Glueer
185 et al., 2019). The great Aletsch glacier is currently retreating at an average rate of ~ 50 m/y
186 for the years 2000-2018 (data from GLAMOS, [http://swiss-glaciers.glaciology.ethz](http://swiss-glaciers.glaciology.ethz.ch)
187 [.ch](http://swiss-glaciers.glaciology.ethz.ch), last accessed November 2020), and its tongue retreated around 3 km since the LIA.
188 Ice downwasting in the study area is in the order of 10 m per year (Hugentobler et al.,
189 2020). The mean annual temperature in the study area is 3.2 ± 0.5 °C at the Chazulecher
190 station (1971 masl, Northwest-facing slope) and 4.6 ± 2.0 °C at the Driest station (2173 masl,
191 Southeast-facing slope) for the period 2013-2020. The mean annual precipitation as mea-
192 sured at the nearby Bruchji station (2300 masl, South-facing slope) since 2013 is 999 ± 139 mm
193 of which a significant proportion falls as snow and accumulates during the cold months.
194 The nearby SLF Eggishorn station (2495 masl, South-facing slope) measured a mean an-
195 nual maximum snow depth of 2.15 ± 0.48 m since 1994, and at the SLF Belalp station
196 (2554 masl, South-facing slope), the mean annual maximum snow depth was 2.52 ± 0.50 m
197 since 2009. For the location of the weather stations used here, see Figure 1 and Table 1.

198
199 The groundwater in the fractured rock mass is fed by water infiltrating from the
200 surface. The availability of water for infiltration is strongly dependent on the temper-
201 ature in alpine environments, as water is stored as snow during most of the winter, with
202 little infiltration, and delivered quickly during snowmelt in spring. Significant ground-
203 water level changes are typically observed at this time of year, resulting in an annual cyclic-
204 ity in groundwater store (de Palézieux & Loew, 2019). During summer, infiltration hap-
205 pens mainly during rainstorms, which are not very frequent, as the climate is dry in the
206 central valleys of the Alps. At the Massa river monitoring station (see Figure 1), the flow
207 in the river fluctuates from low flow in February, with an average of 0.32 ± 0.12 m³/s and
208 extrema around 0.13 m³/s and high flow in July with an average of 44.55 ± 14.88 m³/s
209 and extrema around 97 m³/s (see also Figure A.1). A trend towards earlier snowmelt and

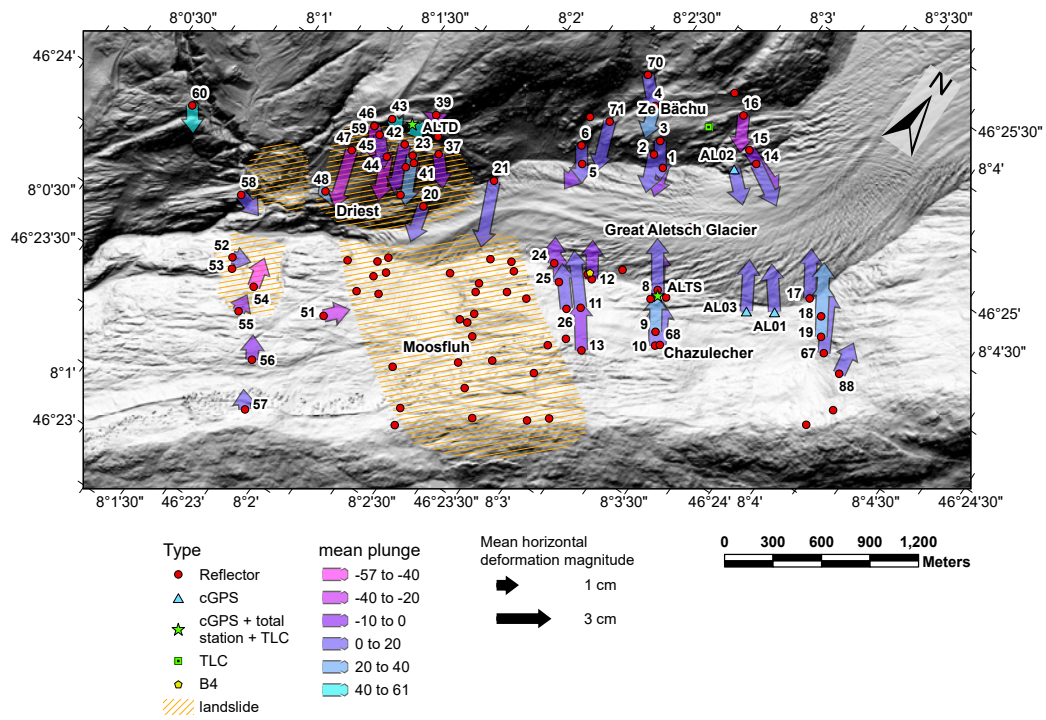


Figure 2. Map of study area with monitoring stations and known slope instabilities. Arrows are the average displacement in Spring exaggerated 10'000 times. Colors of arrows represent the plunge angle. See Figure 1 for the location of this map in a broader context.

210 larger high flows in summer, caused by increased melting of the glacier under the cur-
211 rent climate warming, is predicted in high-alpine catchments (Muelchi et al., 2021).

212 An extensive surface deformation monitoring system was installed in 2013 and con-
213 tinuously expanded and maintained since (Glueer et al., 2020). It includes five contin-
214 uous GPS stations with three different types of monuments. ALTS and ALTD stations
215 are mounted on a 1.5 m high metallic pole of 21 cm diameter, bolted in bedrock (Frukacz
216 et al., 2017). To prevent temperature and wind-related movements of the poles, these
217 are protected by a second larger metallic tube (Frukacz et al., 2017). The monument of
218 the station AL03 consists of a 1 m high and 21 cm in diameter metallic pole bolted in
219 the bedrock. Finally, the stations AL01 and AL02 monuments are described in Limpach
220 et al. (2016).

221 Two total stations were installed on opposite valley flanks directly below the GPS
222 stations of ALTS and ALTD, monitoring their position (see Figure 2). A Leica TPS1200
223 was installed at Chazulecher station, point ALTS, and a Leica TM50 station was installed
224 at Driest, point ALTD (Frukacz et al., 2017; Glueer et al., 2020). These stations track
225 93 reflectors that have been installed on both unstable ground (active landslides) and
226 adjacent stable bedrock (see Figure 2). Reflectors are equipped with a stainless steel roof
227 to protect against snow load, snow creep, and small rockfalls. The air temperature and
228 atmospheric pressure are monitored at the two total stations for data correction, and a
229 nearby weather station is situated in Ze Bächu. In addition, three bedrock monitoring
230 boreholes were drilled in 2017 close to the left glacier margin and described by Hugentobler
231 et al. (2020). Here, only data from borehole B4 are shown. The location of B4 is shown
232 in Figure 2.

233 **3 Data and Methods**

234 **3.1 Surface displacement**

235 The five cGPS stations installed on both flanks of the valley are equipped with low-
236 cost single-frequency GPS devices. The GPS data processing is based on the Bernese GNSS
237 software, using differential carrier phase techniques. Daily static coordinates are com-
238 puted with respect to the geodetic dual-frequency GNSS station FIES situated close to
239 Fiescheralp (Limpach et al., 2016). The relatively short baselines (5.0 km to 7.4 km) be-
240 tween the GPS stations and the reference station FIES allow the mitigation of ionospheric

241 effects by differential processing, and hence the use of single-frequency GPS receivers.
242 The station FIES is part of a regional network of ten geodetic reference stations oper-
243 ated by the Institute of Geodesy and Photogrammetry of ETH Zurich. This regional dual-
244 frequency GNSS network is continuously processed together with stations of the Swiss
245 national network of GNSS reference stations AGNES (Automated GNSS Network for
246 Switzerland) from Swisstopo. The reference station FIES is subject to similar cyclic mo-
247 tions as studied here. Its position is continuously computed with respect to the Swis-
248 stopo station HOHT from the AGNES network, situated in the Rhone valley. This al-
249 lows to eliminate station FIES's motion and to reference the GPS stations near the glacier
250 to the station HOHT in the Rhone valley. A direct vector between the station HOHT
251 and the stations near the glacier would yield much longer baselines prone to ionospheric
252 delay errors with the single-frequency receivers.

253 At the total stations, interruptions of data acquisition sometimes occur during pe-
254 riods where the station is snow or ice-covered and occasionally because of rockfalls or
255 snow avalanches cover or destroy reflectors. Fog in the valley, particularly in autumn,
256 also reduces the visibility of reflectors situated far from the total stations (up to 2 km).
257 Each point is measured multiple times at night, when air temperature gradients along
258 the ray path and wind have a minimal influence on the measurement. The total station
259 records the distance to the reflector, the horizontal angle from North and the vertical
260 angle on each face of the instrument, in order to average the angles obtained and reduce
261 instrumental errors. Then, the measured distance to the prism is corrected for atmospheric
262 temperature effects using correction factors provided by Leica Geosystems AG (2013).

263 Both angles (horizontal and vertical) are low-pass filtered to reduce noise and com-
264 bined with the distance measurement to infer the position of the prism relative to the
265 total station. The station regularly checks its alignment to one of the reflectors, consid-
266 ered as reference, to prevent drift caused by mechanical errors. However, the reference
267 point is not considered as stable and is also included in the analysis here. For ALTD,
268 it is point 39 and for ALTS, point 10 until 2019 and 68 afterwards (see Figure 2). Point
269 68 is located close to 10 but is less often snow-covered, which is important to avoid drift
270 of the angular measurements during winter. Therefore, we decided to include reflector
271 68 as a reference point in 2019. We noticed an increase in instrumental noise when us-
272 ing two reference points and switched to only one (point 68) after a few months. We dis-
273 card data from this period in our statistical analysis to overcome potential issues related

274 to this instrumental noise. We average all night-time measurements between 10 pm and
 275 6 am to calculate daily solutions of each prism position. Because the total station can-
 276 not be considered stable and is subject to a similar motion as the reflectors, we correct
 277 the relative position obtained with the low-pass filtered GPS position of the total sta-
 278 tion to get the absolute position of each prism. For filtering of the position time series,
 279 we apply a Butterworth low-pass filter of third order with a cutting frequency of 3.858×10^{-7} Hz
 280 (corresponding to a period of 1 month, see Figure 3). These parameters are used for low-
 281 pass filtering of daily sampled data throughout this paper if not specified otherwise.

282 The fast displacement in spring (see Figure 3) is calculated for each point with a
 283 peak-to-peak amplitude of the seasonality larger than 5 mm. The points corresponding
 284 to the start and end of the spring displacement are identified on the time series for each
 285 year in the record. We take the average displacement obtained between these two times
 286 for all available years in record, at each point. The results of this analysis is shown in
 287 Figure 2.

288 To extract information from the displacement time series and separate the signal
 289 coming from different temporally independent sources, we use a statistical method, the
 290 Variational Bayesian Independent Component Analysis (vbICA). The vbICA is described
 291 by (Choudrey & Roberts, 2003) and adapted to the study of geodetic position time se-
 292 ries with gaps by Gualandi et al. (2016). We use the two-dimensional horizontal displace-
 293 ment time series (east, north) for reflectors and cGPS stations that do not have large
 294 data gaps (exceeding 20% of the time series). We do not use the vertical component of
 295 displacement, as the noise level is higher in the vertical (see Figure 3), and most of the
 296 displacement is horizontal (see plunge angles in Figure 2). The resulting time series for
 297 each Independent Component (IC) are then compared with environmental variables and
 298 geologic knowledge to explain better the original deformation observed. We select the
 299 number of components to retain via an F-test, and we test different initialization hyper-
 300 parameters. We impose small a priori variance on the mixing matrix hyper-parameters
 301 to stabilize the solution, as described in Gualandi and Liu (2021), e.g. in Table S1. Here
 302 we use values of 1×10^{-3} and 1×10^3 for the hyperparameters b_{α_0} and c_{α_0} respectively.

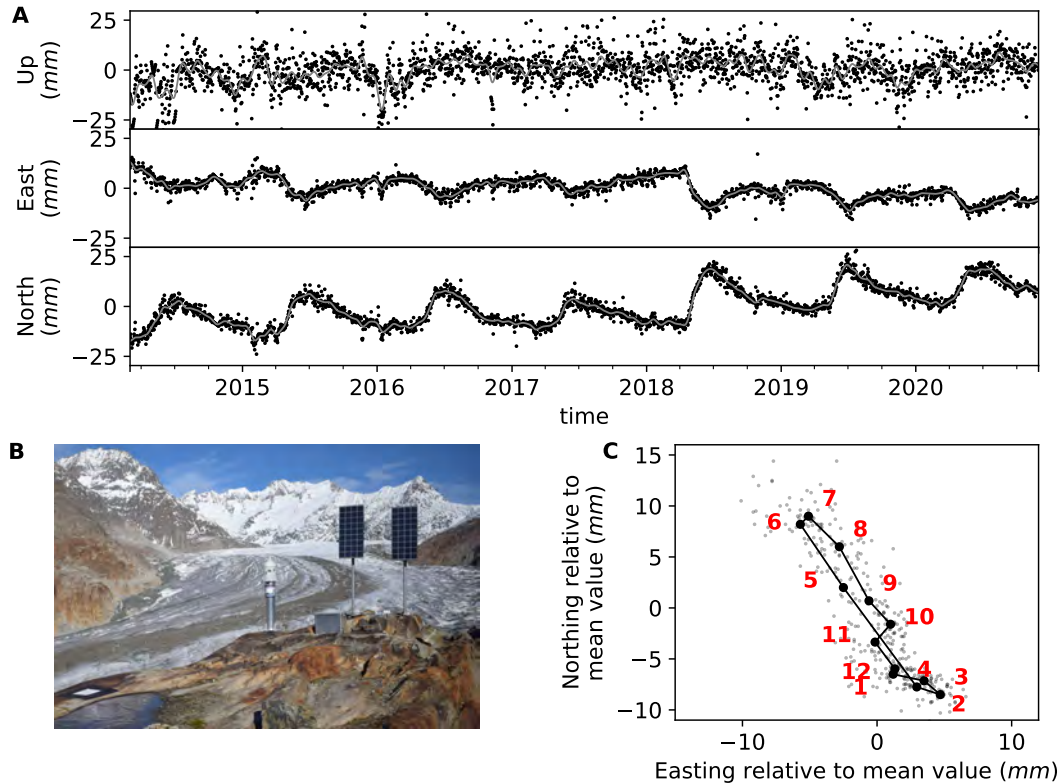


Figure 3. Example of time series for a cGPS situated at the Chazulecher station (ALTS). **A:** three spatial components of displacement relative to HOHT (black dots) with filtered data (grey line) and sinusoidal fit (annual period, red). **B:** picture of the station and its surroundings, view to NE. The GPS is on top of the total station (left mast). **C:** horizontal displacement seen from top. Grey points are average values from ordinal days after linear detrending of the time series. Black points are average monthly values, labeled in red. The quicker deformation in spring to early summer to the NNW is followed by a slower, more gradual deformation in the opposite direction during the rest of the year. The cyclic deformation is mainly in the horizontal direction, although the higher noise in the vertical component might prevent the detection of annual cyclicity.

3.2 Strain analysis

Using the distance measurement of the total station, we can directly infer strain between two points on the slopes. This technique has the advantage of increasing the signal-to-noise ratio, as it does not use the angular calculations of the TPS or the absolute positioning from GPS. For points situated far from the total station, a daily solution of distance measurement is used. High-resolution strain measurements are performed between close reflectors and the total stations. Hourly temperature-corrected distance measurements to the total station, including measurements during the day, offer a dataset similar to the one we would obtain from low-accuracy extensometers. These datasets are used to analyze smaller and shorter relative displacements of the prisms and compared with environmental variables (e.g., air temperature, rainfall, snowfall).

3.3 Weather and climate

Time series of weather variables (air temperature, rainfall, snowfall, atmospheric pressure) are taken from nearby MeteoSwiss stations located outside of the study area (see Table 1). The main stations used are Belalp and Eggishorn. The water level and temperature in the Massa river, at the outlet of the Great Aletsch, Oberaletsch, and Driest glaciers are taken from a station managed by the Federal Office of the Environment (FOEN). Inside the study area, a weather station is installed on the South-facing slope at Ze Bächu and informs on air temperature, atmospheric pressure, bolts of lightning, wind direction and speed, and solar radiation with a 15 minutes sampling interval. Air temperature and atmospheric pressure are also measured at both total stations in Chazulecher and Driest, with an hourly sampling interval.

The spatial variations of snow cover during the melting season are monitored with two time-lapse cameras, each facing one valley flank, using the method described in Aaron et al. (2021). The slopes are partitioned in sectors based on their orientation and elevation characteristics, and the degree-day method (Rango & Martinec, 1995) is applied on each sector, backward in time from the last day with snow in the area, to get an approximate snowmelt timing and amount during the spring snow melting season. A degree-day factor of $0.08 \text{ cm}/(^{\circ}\text{C d})$ is applied during winter and until March and a degree-day factor of $0.4 \text{ cm}/(^{\circ}\text{C d})$ is applied after the start of April, following (Rango & Martinec,

Table 1. Weather data used in this study

Variable	Station	Latitude	Longitude	Altitude (m.a.s.l)
Rainfall	Bruchji	N46° 22' 46"	E007° 58' 18"	2300
Rainfall	Fieschertal	N46° 25' 40"	E008° 08' 28"	1175
Snow height	Belalp	N46° 23' 41"	E007° 58' 27"	2554
Snow height	Eggishorn	N46° 25' 00"	E008° 05' 30"	2495
Temperature	Eggishorn	N46° 25' 00"	E008° 05' 30"	2495
Temperature	Jungfrauoch	N46° 32' 51"	E007° 59' 08"	3571
Massa River flow	Massa - Blatten bei Naters 2161	N46° 23' 08"	E008° 00' 24"	1446

1995). An elevation-dependent temperature correction of $7.2 \times 10^{-3} \text{ }^\circ\text{C/m}$ is applied, based on the temperature gradient observed between nearby measuring stations.

3.4 Groundwater

The variations of groundwater level are monitored in a nearby borehole (Hugentobler et al., 2020), at point B4 (see Figure 2) and are modeled at the catchment scale with the lumped rainfall-runoff model GR5J (Pushpalatha et al., 2011), modified to include a snowmelt routine based on degree-day method (Valéry et al., 2014). The model is calibrated using the variations of stream discharge in the Massa river, with air temperature at the Jungfrauoch, precipitation from the Fieschertal, and solar radiation from the Jungfrauoch station as inputs. GR5J resolves the rainfall partitioning between evapotranspiration, quick (surface) and slow (subsurface) flow paths. From the air temperature and sunshine duration, we calculate the evapotranspiration with the Turc method (Turc, 1961). We use the degree-day method to calculate the snowmelt (Valéry et al., 2014) and we check the validity of the obtained snow store time series with the observed snow depth at the nearby Eggishorn station. The model is calibrated on the river flow at the outlet of the catchment. In the case of the Aletsch valley, the Massa river gauge has a large catchment of $\sim 191 \text{ km}^2$, with many glaciers (see Figure 1). For this reason, the flow in the river is highly influenced by the meltwater from the glaciers, with high flows in summer and a high variability for this time of the year, and low flows in winter (see Figure A.1).

352 We calibrated the GR5J model during winter periods, as the glacier contribution
353 to stream discharge is minimal during these times (see Figure 4). Details of the calibra-
354 tion process are in the appendix. During summer, the strong diurnal variations and high
355 water flow in the Massa river are mainly attributable to melting ice. They peak in the
356 late afternoon and correlate with air temperature in the valley. Additionally, the differ-
357 ence between observed and modeled Massa river flow has a similar order of magnitude
358 as the contribution from the melting of the glacier, which is approximately 10 m of ice
359 loss per year. Differences between the groundwater store modeled and the groundwa-
360 ter head observed in the borehole B4 can be caused by the different scales of observa-
361 tion (see Figure 4). Observed groundwater level variations can be very local, while mod-
362 eled groundwater storage changes are representative of the whole basin. However, relat-
363 ing the groundwater store change in spring (~ 70 mm) with the local water head change
364 in the borehole (~ 15 m) gives an estimated porosity of 0.5 %, which is reasonable for the
365 shallow fractured gneisses and granites of the Aar massif (Masset & Loew, 2010). There-
366 fore, we believe the modeled groundwater store represents the actual groundwater fluc-
367 tuations at the catchment scale for monthly time resolution.

368 **3.5 Geological mapping**

369 Structural field mapping was done using two applications; Fieldmove and Fulcrum.
370 A drone (DJI Phantom v4) was used to acquire a high-resolution surface model around
371 the total station of Chazulecher. The flights were prepared with the software DJI Flight
372 Planner, and Litchi was used to control the drone on-site. Then, the 3D model was com-
373 puted with Agisoft Metashape, and an orthophoto, digital terrain model (DTM), and
374 mesh were produced. Fractures were then manually digitized in ArcGIS Pro from the
375 orthophoto, and shear zones orientations were computed in Virtual Reality Geological
376 Studio (VRGS), and with a hand-held compass in the field.

377 **4 Results**

378 **4.1 Surface Displacement: Temporal and spatial patterns**

379 The installed GPS stations and TPS reflectors record significant reversible and long-
380 term ground surface displacements. On both sides of the glacier, points attached to bedrock
381 exhibit at least three types of motion exceeding the noise level. These are i) reversible

382 short-term displacement, over a few days to a few weeks, ii) annually reversible displace-
383 ment, and iii) apparently irreversible displacement over the period of recording. We ex-
384 clude points from the center of the Moosfluh landslide because the displacement of these
385 points is strongly dominated by the landslide motion and has already been thoroughly
386 studied in a previous paper (Glueer et al., 2020).

387 The three types of motion we observe are well demonstrated by the cGPS station
388 ALTS, shown in Figure 3, in the top three panels. This cGPS station exhibits a long-
389 term trend upwards at an average rate of 1.0 mm/yr, to the North with 3.0 mm/yr and
390 to the West with 1.5 mm/yr over the period 2014-2020. Seasonal cycles with a peak-to-
391 peak amplitude of 24.8 ± 5.7 mm are visible. The seasonal displacement takes place on
392 a plane close to horizontal, but it has to be noted that a higher noise level in the ver-
393 tical component of the cGPS might hide a vertical seasonal displacement component. The
394 bottom right of Figure 3 shows the annual displacement of the GPS antenna in plan view.
395 The East and North components were detrended and averaged per ordinal day (light grey)
396 and month (black dots). The station moves rapidly to the North-West in spring (April
397 to June) and moves back during summer, autumn, and winter (August to December),
398 decreasing velocity over the year. A picture of the station is shown at the bottom left
399 of Figure 3, and the map (Figure 2) indicates that the station is moving towards the val-
400 ley center (i.e., towards the glacier) in spring, and away from it during summer-autumn.

401 The peak-to-peak amplitudes of all points situated outside of the large Moosfluh
402 instability where a seasonal signal was detected are shown as arrows in Figure 2. Most
403 of the points move towards the center of the valley in spring and away from it in summer-
404 autumn. The points that are near each other show similarities, both in terms of direc-
405 tion of motion and magnitude. In general, points on the North-facing slope move to the
406 NNW, and points on the South-facing slope move the SSE with slightly more variation
407 in the direction. Points 14-19 are located where the valley axis is rotating, and the di-
408 rection of motion of these points is not slope-parallel. The points on the North-facing
409 slope seem consistently moving perpendicularly to the orientation of the main alpine fo-
410 liation (mean dip/dip direction of $85^\circ/136^\circ$, see Figure 1). The majority of the points
411 have a plunge angle around 0° ; hence they move almost horizontally. We note that the
412 increased noise in the vertical component of displacement could hide small variations of
413 plunge between points.

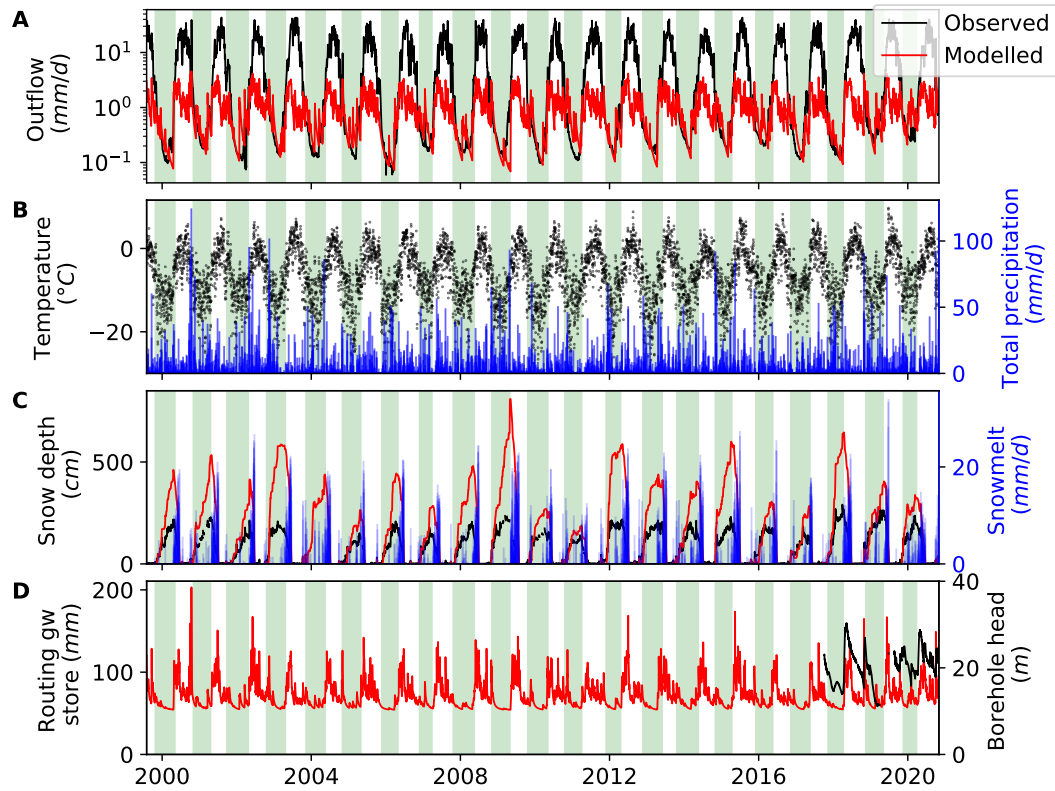


Figure 4. Results of the GR5J model for groundwater store estimation at catchment scale.

A: flow in the Massa river, normalized by the size of the catchment, with observations (black)

and model (red). Calibration periods are shown in green. **B:** temperature at the Jungfrauoch

station (black) and precipitation at the Fiesch station (blue). **C:** snow depth at the Eggishorn

station (black), modeled from GR5J for the entire catchment (red) and modeled snowmelt (blue).

D: groundwater store modeled (red) and observed head in the borehole B4 (black).

414 We extract ICs statistically from the position time series of cGPS and TPS, using
415 the vbICA method. These components can be linearly recombined to explain the obser-
416 vations. We show the results of the vbICA with four ICs on Figure 5. To obtain the con-
417 tribution of each IC to the original data, we have to multiply the spatial distribution (maps
418 in Figure 5) by the corresponding temporal functions. The first IC exhibits a long-term
419 trend, with a strong acceleration in late 2016 and logarithmic deceleration afterward. The
420 timing corresponds to the acceleration phase of the Moosfluh landslide (Glueer et al.,
421 2019), and the map shows that this component is very active for points close to the Moos-
422 fluh instability. Some outliers, as well as some deviations to this trend in 2018, are ob-
423 served. They are considered as caused by noise in the time series. During this time, a
424 data gap affecting both total stations left only the cGPS stations working. The algorithm
425 is affected, and this time period is not representative of the slope motion.

426 The second IC shows a positive long-term trend, as well as cycles with an annual
427 periodicity and variable amplitude between years (see Figure 5). This component is iden-
428 tified at all stations on the map, with a direction towards the center of the valley. The
429 magnitude of the component is increasing towards the Southwest, where the large insta-
430 bilities of Driest and Moosfluh are situated.

431 The third IC shows annual cycles with short positive incursions in spring followed
432 by motion in the opposite direction and a bigger event with opposite direction in 2019
433 (see Figure 5). The magnitude of the component is increasing with the distance to the
434 total station (point ALTS on the map), and the direction exhibits a rotation of the sta-
435 tion around the total station. This peculiar behavior could be caused by a rotation of
436 the station on its axis, with repercussion of this movement to all the reflectors.

437 The fourth IC exhibits similar annual cycles as the second component (see Figure 5
438 and Figure 6) but does not include a long-term trend. The direction of the motion is op-
439 posite to the one of the second IC for points close to the landslides and in the same di-
440 rection as the second IC for other points. The magnitude is larger for points on the North-
441 west facing slope, and point 22 on the Driest landslide. It is possible that both IC2 and
442 IC4 partially describe motion from the same source. IC4 could correct the amplitude of
443 the annual reversible displacement of the points where IC2 could not explain the entire
444 reversible and irreversible signal. For example, points close to the Moosfluh landslide and
445 on the Driest landslide often exhibit opposite directions of motion for IC4 and IC2. There-

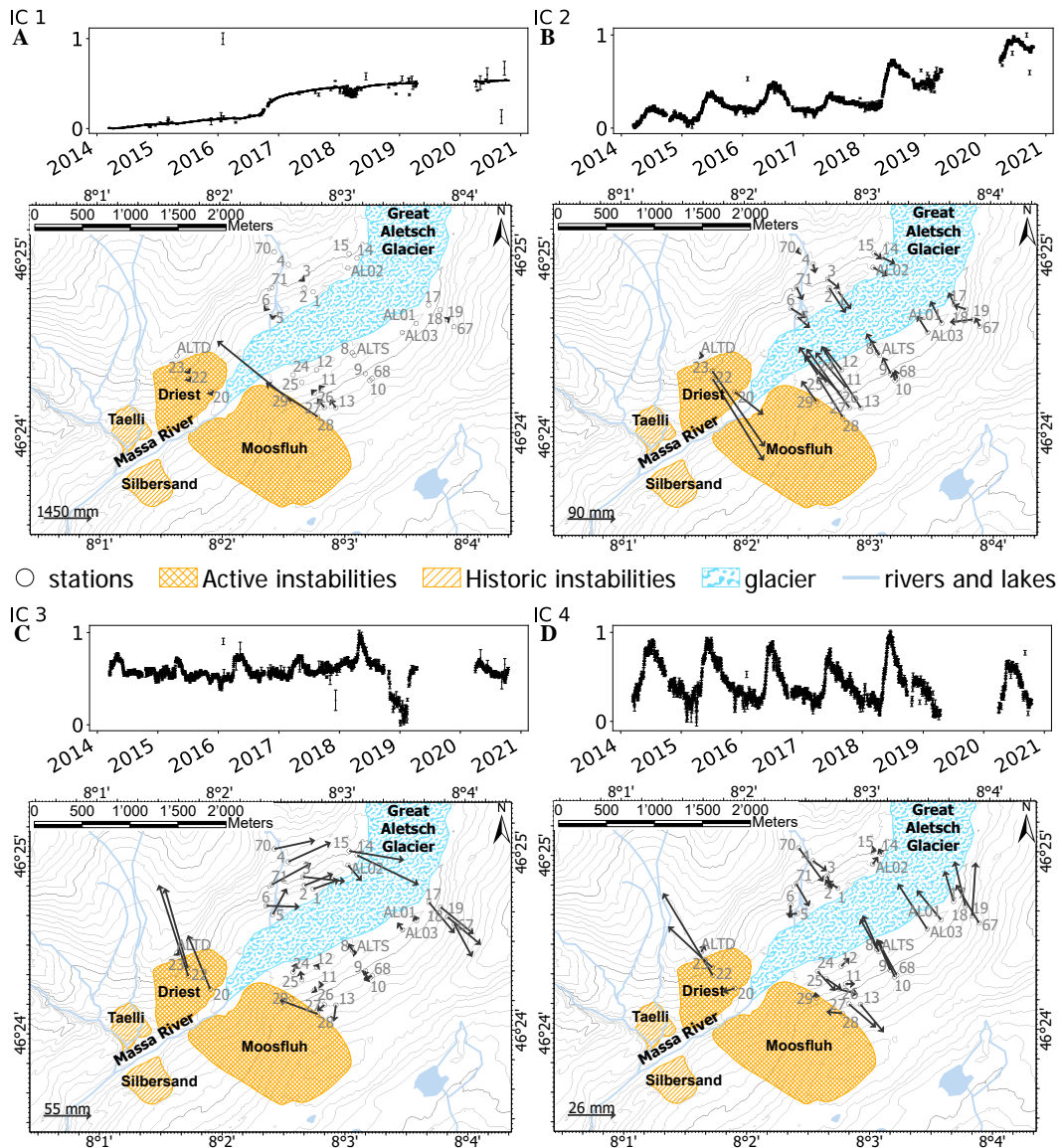


Figure 5. Results of the vbICA analysis with four independent components.

446 fore, IC4 reduces the amplitude of the annual reversible displacement at these points,
447 where IC2 has large amplitudes due to a strong irreversible component of displacement.
448 For the North-East part of the study area, instead, IC4 and IC2 are oriented in a sim-
449 ilar direction. Therefore IC4 serves as a reinforcement of the annual reversible displace-
450 ment where IC2 exhibits lower amplitudes, because the irreversible component of dis-
451 placement is smaller at these points. Both components could represent a single source
452 responsible for both annually reversible and irreversible displacements, or of two sepa-
453 rate sources that are difficult to differentiate.

454 In Figure 6, we show resulting groundwater storage variations obtained from the
455 GR5J model, corresponding to estimated catchment-scale groundwater store variations.
456 Seasonal cycles are caused by increased infiltration and recharge during snowmelt in spring.
457 During summer, autumn, and winter, the groundwater store is depleting. Interannual
458 variations in the magnitude of groundwater store variations are linked to different to-
459 tal Snow-Water Equivalent (SWE) in the snowpack between years. The calibration pe-
460 riods of the model are in green in Figure 4. The ICs 2 and 4, exhibiting the annual cy-
461 cles, are shown in figure 6. There is a good match between the general trend of monthly
462 catchment-scale groundwater storage and deformation in the study area, both in terms
463 of timing and inter-annual magnitude variations. Pearson’s correlation coefficient between
464 groundwater store and the ICs 2 and 4 of ground deformation are respectively 0.37 and
465 0.77 at a monthly resolution. The long-term trend in IC2 reduces the correlation coef-
466 ficient with the groundwater store.

467 **4.2 Strain measurements**

468 In Figure 7, we show strain measured across the valley, from the Chazulecher to-
469 tal station to the reflector point number 2. We choose this reflector because its direc-
470 tion from the total station is parallel to the main direction of annually cyclic deforma-
471 tion in this part of the valley (see Figure 2) and because it has relatively few periods of
472 missing data. Also, the strain across the valley integrates the deformation from both slopes,
473 increasing the amplitude of the annual cycles and the signal-to-noise ratio. A clear long-
474 term trend is visible, with a shortening of the distance between these two points of 11.3 mm/yr
475 on average between 2014 and 2020. The annual reversible cycles described in the pre-
476 vious section are again evident in this dataset, with a shortening every year in spring fol-
477 lowed by extension during the rest of the year. The magnitude of deformation in spring

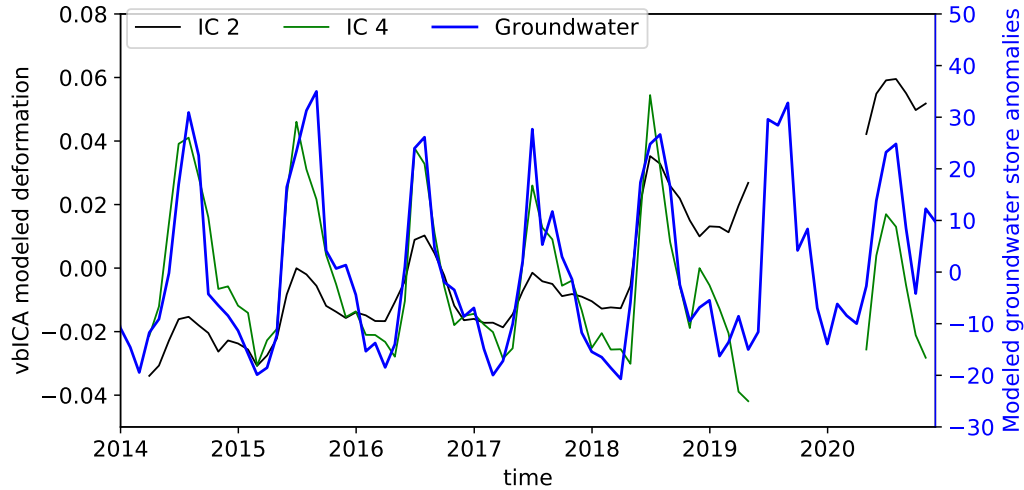


Figure 6. Comparison between the ground deformation extracted from the vbICA method (IC2, black and IC4, green) and groundwater estimated with the GR5J model (blue), normalised with the mean and standard deviation of the timeseries.

478 can be related to the magnitude of non-recovered deformation, calculated from winter
 479 times each year (see Table 2). The deformation of the valley in spring is synchronous with
 480 the onset of snowmelt in the valley, as shown in Figure 7. However, the subsequent open-
 481 ing of the valley starts well before the snow begins to accumulate again on the slopes,
 482 discarding loading of the surface by snow accumulation has the main driver of the de-
 483 formation. The temperature is also shown in Figure 7. The Pearson’s correlation coef-
 484 ficient between strain and temperature is -0.39 , and seasonality is visible for both vari-
 485 ables. However, the asymmetry in the deformation signal is not reproduced in the tem-
 486 perature, which exhibits a more sinusoidal shape in general. In addition, some small re-
 487 versible incursions in strain (marked with stars in Figure 7) cannot be related to changes
 488 in air temperature or snowpack. These seem to be linked to periods of heavy rainfall with
 489 a shortening after storms, in spring to autumn.

490 The groundwater level in the 50 m deep borehole B4 is measured in the middle of
 491 the North-facing slope and is shown in Figure 8 (red curve). The groundwater level rises
 492 during snowmelt in spring and early winter and heavy rainfall in summer and autumn
 493 when snow-free conditions prevail. The comparison with ground deformation between
 494 the total station and reflector number 8 on the same slope exhibits a good match with
 495 the groundwater level in the borehole (Pearson’s correlation coefficient of 0.74). During

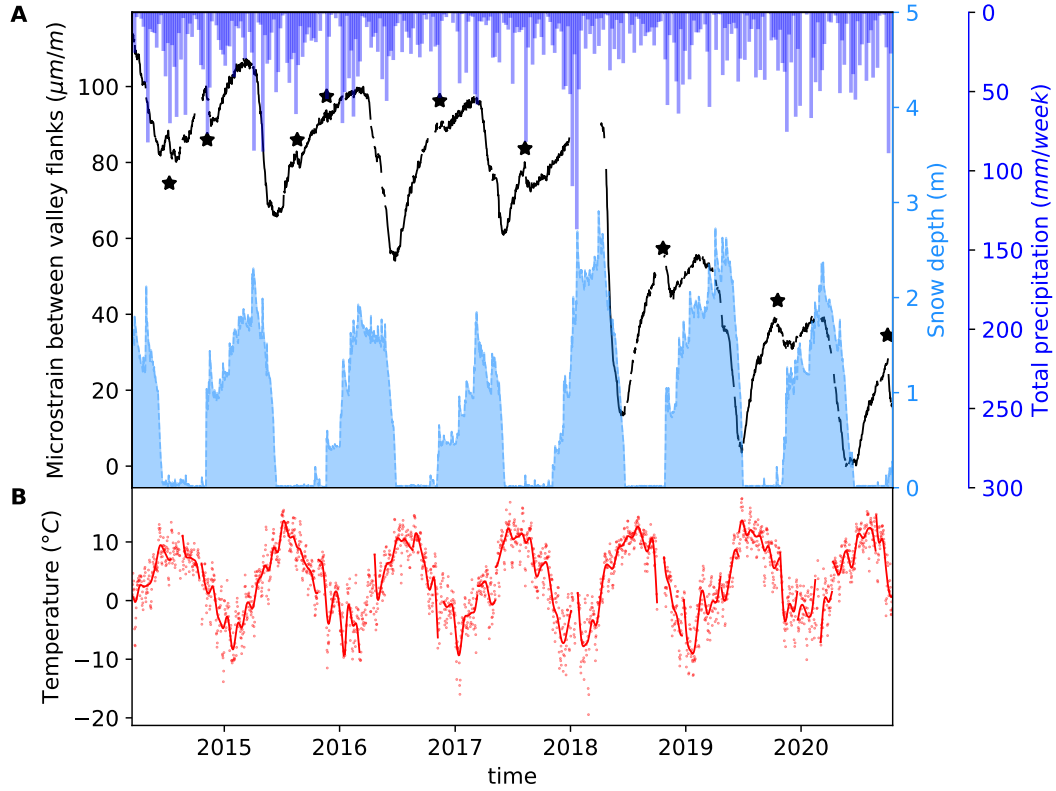


Figure 7. **A:** Distance measurement timeseries, between two points on each side of the valley (here, reflector number 2 and the total station in Chazulecher, black). The distance measurement is corrected for effect of air temperature, atmospheric pressure and air humidity. Snow depth (light blue, Eggishorn MeteoSwiss station) and rainfall per day (deep blue, Bruchji Meteoswiss station) are also shown, as well as short periods of deformation during summer/autumn (stars). **B:** Daily mean temperature (points) and low-pass filtered data (line) at the Chazulecher station.

Table 2. Reversible and irreversible displacement across the valley

Year	Spring deformation (microstrains)	Annual non-recovered deformation (microstrains)
2015	41	7
2016	46	3
2017	36	7
2018	76	35
2019	51	16
2020	39	11

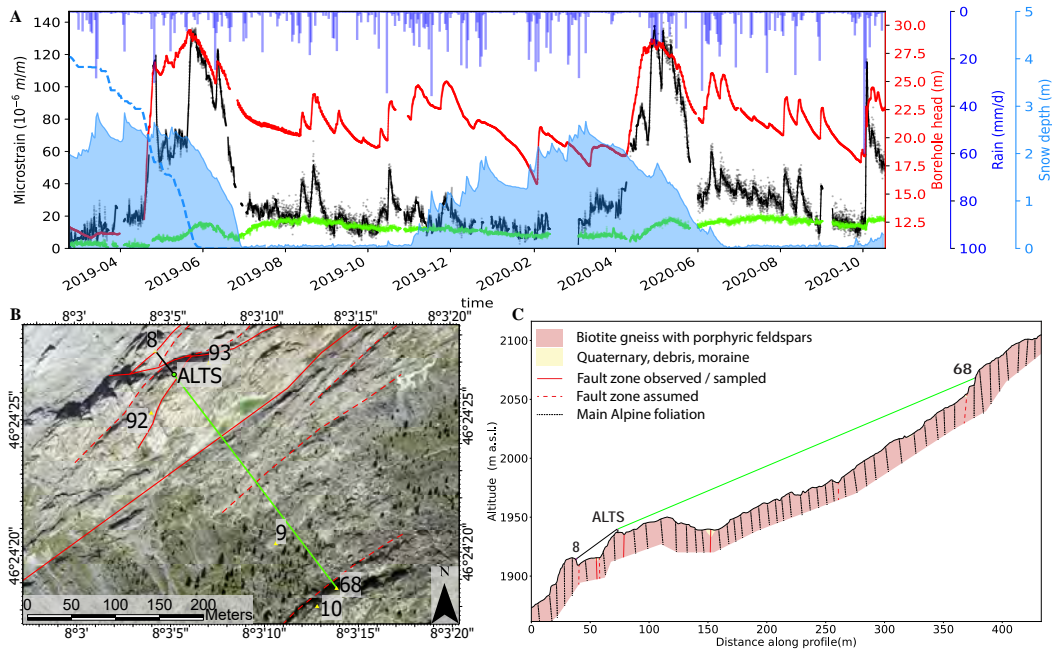


Figure 8. **A:** Comparison between the ground deformation (black, reflector 8, green, reflector 68) and the groundwater head in a borehole (red, B4). Rainfall (blue, Bruchji) and snow depth (light blue fill, Eggishorn) are also shown. The dashed dodgerblue line is local SWE around B4 estimated from a time-lapse camera in 2019 (exaggerated ten times for comparison with snow depth). The camera was not recording in spring 2020 due to technical issues. **B:** Map and **C:** simplified geologic profile view showing the two lines to reflectors 8 (black) and 68 (green).

496 winter, exceptions are observed when relatively quick drops in the borehole head with
 497 an unusual acceleration over time are not seen in the deformation time series. The de-
 498 formation between the total station and the reflector 68 is smaller than between the to-
 499 tal station and reflector 8, with a much smaller reaction to heavy rainfall events and snowmelt
 500 periods. However, the lines to these two points are oriented in the same direction, and
 501 the general slope of the surface is similar for both stations (see Figure 8). We observe
 502 large fault zones, generally oriented parallel to the alpine foliation, and we identify sev-
 503 eral fault zones crossing the two investigated lines. We note that the density of mapped
 504 fault zones is much larger for the section to the reflector 8 than the one to the reflector
 505 68 (see Figure 8).

5 Discussion

5.1 Driving factors for reversible slope deformations

Deformation signals monitored at different locations worldwide have been hypothesized to be controlled by hydromechanical processes linked to the variation in pore pressure. For example, in the Gotthard tunnel in the central Swiss Alps (Loew et al., 2007; Hansmann et al., 2012) and at the long valley caldera in the USA (Silverii et al., 2020), as well as previous studies in the Aletsch valley (Grämiger et al., 2020; Hugentobler et al., 2020). Here, we show a correlation between surface deformation and groundwater storage variations that confirms this hypothesis. We systematically find this control at different spatial and temporal scales, from the borehole to the slope scale and from the rainfall event to the seasonal hydrological cycle. Notably, we find Pearson's correlation coefficients of 0.77 and 0.74 between respectively the IC4 and the groundwater storage from the GR5J model and the groundwater head monitored in the borehole B4 and a nearby reflector (point 8). We can confirm that hydromechanical processes linked to the variation in pore pressure control the deformation patterns. At the annual timescale, the ground deformation follows an exponential decay, similarly to the diffusion of pressure during the drainage of an aquifer, with an estimated characteristic diffusive timescale of the order of one month (Brutsaert & Nieber, 1977; Roques et al., 2021).

While the temperature was observed to drive ground deformation in other places of the Alps (see Section 1 and references therein), modeled thermoelasticity in the Aletsch valley and elsewhere only results in around a millimeter-scale surface deformation (Grämiger et al., 2018). The thermoelastic deformation is expected to influence the measured strain for periods without snow cover insulating the ground, with expansion of the near-surface rocks during warming, resulting in shortening distance across valley flanks in spring, thus adding to the hydromechanical deformation (see Figure 7). However, our results suggest that strong diurnal variations in temperature do not induce significant strain during summer (see e.g. Figure 8) and that the annual peak of deformation systematically occurs before the maximum temperature. Furthermore, the displacement and the strain show a different temporal pattern with respect to temperature, with clear non-sinusoidal behavior. Therefore, we demonstrate that temperature remains a minor driving factor of deformation at the study site.

537 As mentioned in Section 1, frost-heave in open fractures can also be expected to
538 drive surface deformation. In Aletsch, the rainfall-related deformation occurs with only
539 positive temperatures, excluding frost as a possible driver of this motion. Furthermore,
540 we do not identify episodes of expansion in early winter, and the snowmelt is associated
541 with periods of heave, countering any possible effect of ice thawing in open fractures (see
542 Figure 7).

543 Hygroscopic expansion happens in meso- and macro-porous material like micro-
544 cracks in gneisses and granites. Hockman and Kessler (1950) have shown that wetting
545 an intact granite in the laboratory leads to an elastic extensional strain of typically 4×10^{-5}
546 (40 microstrains), which is of similar magnitude to the annual cyclic strains recorded in
547 the study area (see Table 2). Near-surface wetting of dry gneisses and granites could oc-
548 cur during rainstorms and possibly snowmelt. However, the time-dependent strains recorded
549 during wetting and drying laboratory experiments (e.g. Hockman & Kessler, 1950) oc-
550 cur on much shorter time scales (e.g. hours) than the annual cyclic deformations mon-
551 itored in the Aletsch valley. It suggests that the dominant strain signals are related to
552 pressure diffusion and the hydromechanical response of macroscopic permeable struc-
553 tures such as fault zones.

554 We explore the possibility that a part of the annual elastic deformation observed
555 in the Aletsch valley is caused by the winter snowpack loading the ground surface. We
556 note that the deformation of stiff fractured granite and gneisses is about three orders of
557 magnitudes smaller than for soils. 3 m of average snow depth corresponds to an addi-
558 tional pressure of around 15 kPa on the ground (assuming a snow density of $\sim 500 \text{ kg/m}^3$).
559 The snow covers the entire surface, adding a relatively homogeneous load on the ground,
560 although strong spatial variations are observed, with accumulation in depressions and
561 below steep walls, as well as on preferential slope orientations (Lundberg et al., 2016).
562 For a fractured elastic material of 20 GPa stiffness in the active layer (the top 200 m),
563 the resulting vertical strain is minimal ($\sim 0.1 \text{ mm}$), with progressive subsidence during
564 winter when snow accumulates, and uplift during snowmelt. In mountains, the hetero-
565 geneity of snow accumulation due to steep rock faces could induce a minor horizontal
566 component of strain, oriented towards the valley in winter and in the opposite direction
567 during snowmelt. Such small deformations are below the capabilities of our monitoring
568 system. The strain across the valley (Figure 7), as well as the strain between two points
569 of the same slope (Figure 8) do not exhibit a significant change during the first part of

570 the winter when snow accumulates. Thus, the surface deformation by loading from snow
 571 appears negligible at our study site.

572 Among the possible drivers of reversible slope deformation, groundwater-related
 573 effect is predominant, as it can explain both seasonal cyclic deformation and short-term
 574 excursions following heavy rainfall. We do not exclude other possible drivers but believe
 575 their effects are minor compared to varying the groundwater content and water table el-
 576 evation in the slopes.

577 **5.2 Controls on the spatial variations in reversible deformation**

578 The spatial variations of the annually reversible deformation shown in Figure 2 demon-
 579 strate that all reflectors on both sides of the valley move towards the center of the val-
 580 ley in spring, during snowmelt. The orientation of the motion is relatively homogeneous
 581 throughout the study area, except for a zone in the North (points 14, 15, 16, AL02) and
 582 a zone in the Southwest (points 51-55), where some deviations are visible. The latter group
 583 of points is located close to an active landslide, which affects the orientation of the de-
 584 formation, and the magnitude of the deformation is relatively small, decreasing the signal-
 585 to-noise ratio and increasing the uncertainty in the orientation. In the former area (points
 586 14-16, AL02), the valley axis is also rotating, possibly indicating an influence of the to-
 587 pography on the orientation of deformation. However, on the other side of the glacier,
 588 the slope orientation is rotated too, but displacements observed at points 17, 18, 19, and
 589 AL01 are not perpendicular to the average slope angle around these points. Instead, the
 590 displacement direction for this group of points is consistent with the direction of the other
 591 points on this side of the valley, with an average horizontal orientation of $328 \pm 7^\circ$. The
 592 main alpine foliation has an average dip and dip direction of $85^\circ/137^\circ$ in the valley, with
 593 traces of associated shear zones partly visible with the digital terrain model of Figure 2.
 594 Hence, the slope is moving perpendicularly to the Alpine foliation and faulting each year.

595 Figure 8 exhibits details of spatial and temporal differences in deformation at small-
 596 scale for points situated on the same slope. We show that the response to recharge is het-
 597 erogeneous in space, with stronger deformation of the line between the reflector 8 and
 598 the total station (up to around 100 microstrains for a strong storm event in October 2020)
 599 as between the total station and the reflector 68 (only 6 microstrains for the same storm,
 600 starting more than 12 h after the start of ground reaction to point 8). Similarly, during

601 snowmelt, the part of the slope towards point 8 reacts quicker and more than the other
 602 line. While the distance between the total station and point 8 (42.6 m) is much smaller
 603 than the distance to point 68 (331.0 m), the density of fault zones between the points
 604 is larger for the former line. Because the lithology and orientation of foliation are sim-
 605 ilar for both regions, we believe the fault zones are key to explain the spatial and tem-
 606 poral differences in groundwater-related deformation. We show that the line to the re-
 607 flector 8 exhibits a quick response to infiltration, and a similar recession as the pressure
 608 sensor in the borehole (at ~ 50 m below ground), while the line to the reflector 68 shows
 609 a smaller, slower reaction to summer rainstorms. In addition, both lines exhibit annual
 610 cycles with slow recession following snowmelt. The differences highlighted in responses
 611 to infiltration and recession shapes could be caused by heterogeneity in the average hy-
 612 draulic conductivity of the rockmass.

613 **5.3 Drivers for long-term trends and rock mass fatigue**

614 The cGPS stations in this study exhibit a trend with an uplift of respectively 0.7 mm/yr
 615 (ALTD), 1.0 mm/yr (ALTS), 1.6 mm/yr (AL01), 2.6 mm/yr (AL02) compared to the up-
 616 lift of the reference station Hohtenn (HOHT). The station HOHT, situated in the Rhone
 617 valley, also has an uplift rate of around 2.1 mm/yr relative to the swiss coordinate ref-
 618 erence system CHTRF2016 (<http://pnac.swisstopo.admin.ch/pages/en/chtrf.html>,
 619 last accessed March 2021). We observe that the rates described in this study are in line
 620 with previous uplift rates observed in the region (Sternai et al., 2019), and are partic-
 621 ularly high for stations closer to the Aletsch glacier. It is expected that the elastic re-
 622 bound to the current melting of the glacier has a relatively short distance of influence
 623 (e.g. Sternai et al., 2019). We indeed find that cGPS stations situated closer to the glacier
 624 show larger uplift rates (e.g. AL01, AL02, AL03, ALTS) than stations further away from
 625 the current ice body (e.g. ALTD).

626 We also observe long-term trends towards valley closing, e.g. in Figure 7 and in Fig-
 627 ure 5, for the independent components 1 and 2. In Figure 7, the rate of closure is around
 628 $14.4 \mu\text{strain/yr}$, or 12.6 mm/yr . The irreversible horizontal deformation observed seems
 629 to be consistent with damage modeling results of paraglacial slopes under long-term hy-
 630 dromechanical forcing during strong glacier retreat (Grämiger et al., 2020). In addition,
 631 it seems that an individual snowmelt season can influence the long-term irreversible de-
 632 formation of the slope (see, for example, Figure 7). We observe a larger displacement

633 during the 2018 snowmelt season for all monitoring points, and this displacement was
634 not entirely recovered in the following year (see IC 2 on Figure 5). In fact, for the line
635 shown in Figure 7, the trend between October 17 2014 and October 17 2017 is $6.2 \mu\text{strain}/\text{year}$
636 (against $14.4 \mu\text{strain}/\text{year}$ if taken until October 17 2020). We then hypothesize that strong
637 groundwater storage variations caused by high snowmelt infiltration rates may be plau-
638 sible causes for most of the irreversible deformation. Hydromechanical fatigue could lead
639 to slip along slope parallel preexisting fractures under low effective normal stresses or
640 subcritical propagation of fractures under elevated gravitational shear stress. This ob-
641 servation suggests that part of the observed long-term trend causing valley closing may
642 be related to hydromechanically-controlled slope fatigue, superimposed to the effect of glacier
643 retreat.

644 **6 Conclusions**

645 This study describes and analyzes a large dataset of surface deformation in the Aletsch
646 Valley, Valais, Switzerland, based on two total stations monitoring 93 reflectors, and five
647 continuous GPS stations. The measurements started in the first half of 2014 and are still
648 ongoing in 2021. The time series of these data sets exhibit both long-term deformation
649 trends and annually cyclic displacements.

650 We can show that the annually cyclic displacements:

- 651 • are oriented towards the valley center and perpendicular to the main alpine fo-
652 liation during spring at almost all stations where this type of motion could be ob-
653 served (Figure 2).
- 654 • show a peak-to-peak displacement magnitude of up to 3.8 cm (Figures 3 and 2).
- 655 • correlate in magnitude with snow height and (meltwater equivalent) at the begin-
656 ning of spring groundwater recharge period
- 657 • are correlated to groundwater storage/table variations estimated with a simple lumped
658 rainfall-runoff model, as well as subsurface pore pressure measurements. (Figure 6).

659 Groundwater-induced surface displacements can also be observed following short-term
660 recharge periods, such as summer rainfall events (Figure 7 and Figure 8). Both the an-
661 nual displacement caused by spring snowmelt and short-term displacements caused by
662 rainfall events correlate with groundwater level time series in a nearby borehole. There-

663 fore, we conclude that the reversible surface displacements are mainly caused by vari-
664 ations of a phreatic groundwater level in the granitic and gneissic rock mass. Minor ad-
665 ditional contributions from thermoelastic strains, hygroscopic expansion and snow load-
666 ing of the ground can not be excluded, but we show that these effects must induce only
667 small displacement magnitudes in the Aletsch valley.

668 In the study area, the deformation is relatively homogeneous at large-scale (Fig-
669 ure 2), but can exhibit significant variations locally (Figure 8). Short-distance measure-
670 ments show that deformation is heterogeneous in space, with substantially increased strain
671 close to steeply dipping brittle-ductile fault zones. We hypothesize that some of the larger-
672 scale fault zones are a significant source of groundwater-induced strain in the slopes.

673 Long-term trends in the surface displacement time series are observed consisting
674 of i) long-term differential uplift close to the glacier border (in the order of 1 mm/yr to
675 3 mm/yr) and ii) horizontal slope displacements (in the order of 1 mm/yr to 10 mm/yr
676 for points out of mapped active instabilities) leading to a progressive closure of the val-
677 ley (see Figures 3 and 7). The first trend can be related to isostatic elastic rebound af-
678 ter long term glacier ice downwasting. The irreversible horizontal displacements can be
679 explained by slope damage and shear along critically oriented fractures, driven by rock
680 mass fatigue from annual hydromechanical loading. We can relate the magnitude of peak-
681 to-peak annual displacement with the amount of non-recovered displacement per year
682 for measurements across the valley (Figure 7 and Table 2). Longer time series and fur-
683 ther investigations are needed to confirm this hypothesis.

684 **Acknowledgments**

685 This project is funded by the Swiss National Science Foundation (project 172492). The
686 displacement data used in this study will be made available through the ETH Research
687 Collections once accepted. We thank Franziska Glueer and Reto Seifert for installing most
688 of the monitoring system and Andrea Manconi for helping with the maintenance. We
689 thank the many field helpers who gave some time for this project through the years. There
690 would not be enough space here to name them all. We thank Bernadette "Berni" Würsch
691 and Andrea Gossweiler, as well as colleagues and friends for all the great discussions.

692 **References**

- 693 Aaron, J., Loew, S., & Forrer, M. (2021, 3). Recharge response and kinematics
 694 of an unusual earthflow in Liechtenstein. *Landslides*(November 2020). Re-
 695 trieved from <http://link.springer.com/10.1007/s10346-021-01633-5> doi:
 696 10.1007/s10346-021-01633-5
- 697 Berger, A., Mercolli, I., Herwegh, M., & Gnos, E. (2016). *Geological Map of the Aar*
 698 *Massif, Tavetsch and Gotthard Nappes. - Geol. spec. Map 1:100000, map sheet*
 699 *129*. Wabern: Federal Office of Topography swisstopo.
- 700 Bettinelli, P., Avouac, J. P., Flouzat, M., Bollinger, L., Ramillien, G., Rajaure, S., &
 701 Sapkota, S. (2008). Seasonal variations of seismicity and geodetic strain in the
 702 Himalaya induced by surface hydrology. *Earth and Planetary Science Letters*.
 703 doi: 10.1016/j.epsl.2007.11.021
- 704 Biot, M. A. (1941, 2). General Theory of Three-Dimensional Consolidation.
 705 *Journal of Applied Physics*, 12(2), 155–164. Retrieved from [http://](http://aip.scitation.org/doi/10.1063/1.1712886)
 706 aip.scitation.org/doi/10.1063/1.1712886 doi: 10.1063/1.1712886
- 707 Braitenberg, C., Pivetta, T., Barbolla, D. F., Gabrovšek, F., Devoti, R., & Nagy, I.
 708 (2019, 12). Terrain uplift due to natural hydrologic overpressure in karstic con-
 709 duits. *Scientific Reports*, 9(1), 3934. Retrieved from [http://www.nature.com/](http://www.nature.com/articles/s41598-019-38814-1)
 710 [articles/s41598-019-38814-1](http://www.nature.com/articles/s41598-019-38814-1) doi: 10.1038/s41598-019-38814-1
- 711 Brutsaert, W., & Nieber, J. L. (1977, 6). Regionalized drought flow hydrographs
 712 from a mature glaciated plateau. *Water Resources Research*, 13(3), 637–643.
 713 Retrieved from <http://doi.wiley.com/10.1029/WR013i003p00637> doi: 10.
 714 .1029/WR013i003p00637
- 715 Chanard, K., Avouac, J. P., Ramillien, G., & Genrich, J. (2014). Modeling defor-
 716 mation induced by seasonal variations of continental water in the Himalaya
 717 region: Sensitivity to Earth elastic structure. *Journal of Geophysical Research:*
 718 *Solid Earth*, 119(6), 5097–5113. doi: 10.1002/2013JB010451
- 719 Choudrey, R. A., & Roberts, S. J. (2003, 1). Variational Mixture of
 720 Bayesian Independent Component Analyzers. *Neural Computa-*
 721 *tion*, 15(1), 213–252. Retrieved from [http://www.scopus.com/](http://www.scopus.com/inward/record.url?eid=2-s2.0-0037270849&partnerID=40&md5=9884070ef680ceba2ecc3990cff1744b)
 722 [inward/record.url?eid=2-s2.0-0037270849&partnerID=40&md5=](http://www.scopus.com/inward/record.url?eid=2-s2.0-0037270849&partnerID=40&md5=9884070ef680ceba2ecc3990cff1744b)
 723 [9884070ef680ceba2ecc3990cff1744b](http://www.mitpressjournals.org/doi/10.1162/089976603321043766)[http://www.mitpressjournals.org/](http://www.mitpressjournals.org/doi/10.1162/089976603321043766)
 724 [doi/10.1162/089976603321043766](http://www.mitpressjournals.org/doi/10.1162/089976603321043766) doi: 10.1162/089976603321043766

- 725 Cody, E., Anderson, B. M., McColl, S. T., Fuller, I. C., & Purdie, H. L. (2020,
726 12). Paraglacial adjustment of sediment slopes during and immediately
727 after glacial debuttressing. *Geomorphology*, 371, 107411. Retrieved
728 from <https://doi.org/10.1016/j.geomorph.2020.107411>[https://](https://linkinghub.elsevier.com/retrieve/pii/S0169555X20303846)
729 linkinghub.elsevier.com/retrieve/pii/S0169555X20303846 doi:
730 10.1016/j.geomorph.2020.107411
- 731 Collins, B. D., & Stock, G. M. (2016, 3). Rockfall triggering by cyclic thermal
732 stressing of exfoliation fractures. *Nature Geoscience*, 9, 395. Retrieved from
733 <https://doi.org/10.1038/ngeo2686><http://10.0.4.14/ngeo2686>[https://](https://www.nature.com/articles/ngeo2686#supplementary-information)
734 www.nature.com/articles/ngeo2686#supplementary-information
- 735 Collins, B. D., Stock, G. M., Eppes, M. C., Lewis, S. W., Corbett, S. C., & Smith,
736 J. B. (2018). Thermal influences on spontaneous rock dome exfoliation. *Nature*
737 *Communications*, 9(1), 1–12. Retrieved from [http://dx.doi.org/10.1038/](http://dx.doi.org/10.1038/s41467-017-02728-1)
738 [s41467-017-02728-1](http://dx.doi.org/10.1038/s41467-017-02728-1) doi: 10.1038/s41467-017-02728-1
- 739 de Palézieux, L., & Loew, S. (2019, 12). Long-term transient groundwater
740 pressure and deep infiltration in Alpine mountain slopes (Poschiavo Val-
741 ley, Switzerland). *Hydrogeology Journal*, 27(8), 2817–2834. Retrieved
742 from <http://link.springer.com/10.1007/s10040-019-02025-9> doi:
743 10.1007/s10040-019-02025-9
- 744 Drouin, V., Heki, K., Sigmundsson, F., Hreinsdóttir, S., & Ófeigsson, B. G. (2016).
745 Constraints on seasonal load variations and regional rigidity from continuous
746 GPS measurements in Iceland, 1997–2014. *Geophysical Journal International*,
747 205(3), 1843–1858. doi: 10.1093/gji/ggw122
- 748 Eberhardt, E., Stead, D., & Coggan, J. (2004, 1). Numerical analysis of initia-
749 tion and progressive failure in natural rock slopes—the 1991 Randa rockslide.
750 *International Journal of Rock Mechanics and Mining Sciences*, 41(1), 69–
751 87. Retrieved from [https://linkinghub.elsevier.com/retrieve/pii/](https://linkinghub.elsevier.com/retrieve/pii/S1365160903000765)
752 [S1365160903000765](https://linkinghub.elsevier.com/retrieve/pii/S1365160903000765) doi: 10.1016/S1365-1609(03)00076-5
- 753 Flouzat, M., Bettinelli, P., Willis, P., Avouac, J.-P., Héritier, T., & Gautam, U.
754 (2009, 9). Investigating tropospheric effects and seasonal position variations in
755 GPS and DORIS time-series from the Nepal Himalaya. *Geophysical Journal*
756 *International*, 178(3), 1246–1259. Retrieved from [http://dx.doi.org/](http://dx.doi.org/10.1111/j.1365-246X.2009.04252.x)
757 [10.1111/j.1365-246X.2009.04252.x](http://dx.doi.org/10.1111/j.1365-246X.2009.04252.x)<https://academic.oup.com/>

- 758 [gji/article-lookup/doi/10.1111/j.1365-246X.2009.04252.x](https://doi.org/10.1111/j.1365-246X.2009.04252.x) doi:
759 10.1111/j.1365-246X.2009.04252.x
- 760 Frukacz, M., Presl, R., Wieser, A., & Favot, D. (2017). Pushing the sensitivity limits
761 of RTS-based continuous deformation monitoring of an alpine valley. *Applied*
762 *Geomatics*, 9(2), 81–92. Retrieved from <https://doi.org/10.1007/s12518-017-0182-2>
763 doi: 10.1007/s12518-017-0182-2
- 764 Gahalaut, V. K., Yadav, R. K., Sreejith, K. M., Gahalaut, K., Bürgmann, R.,
765 Agrawa, R., ... Bansal, A. (2017). InSAR and GPS measurements of crustal
766 deformation due to seasonal loading of Tehri reservoir in Garhwal Himalaya,
767 India. *Geophysical Journal International*. doi: 10.1093/gji/ggx015
- 768 Gautam, P. K., Gahalaut, V., Prajapati, S. K., Kumar, N., Yadav, R. K., Rana, N.,
769 & Dabral, C. P. (2017, 12). Continuous GPS measurements of crustal deforma-
770 tion in Garhwal-Kumaun Himalaya. *Quaternary International*, 462, 124–129.
771 Retrieved from [https://www.sciencedirect.com/science/article/pii/
772 S1040618216307017?via%3Dihub#fig2https://linkinghub.elsevier.com/
773 retrieve/pii/S1040618216307017](https://www.sciencedirect.com/science/article/pii/S1040618216307017?via%3Dihub#fig2https://linkinghub.elsevier.com/retrieve/pii/S1040618216307017) doi: 10.1016/j.quaint.2017.05.043
- 774 Girard, L., Gruber, S., Weber, S., & Beutel, J. (2013). Environmental controls of
775 frost cracking revealed through in situ acoustic emission measurements in steep
776 bedrock. *Geophysical Research Letters*, 40(9), 1748–1753. Retrieved from
777 <https://agupubs.onlinelibrary.wiley.com/doi/abs/10.1002/grl.50384>
778 doi: 10.1002/grl.50384
- 779 Gischig, V. S., Moore, J. R., Evans, K. F., Amann, F., & Loew, S. (2011). Ther-
780 momechanical forcing of deep rock slope deformation: 2. The Randa rock
781 slope instability. *Journal of Geophysical Research: Earth Surface*, 116(F4).
782 Retrieved from [https://agupubs.onlinelibrary.wiley.com/doi/abs/
783 10.1029/2011JF002007](https://agupubs.onlinelibrary.wiley.com/doi/abs/10.1029/2011JF002007) doi: 10.1029/2011JF002007
- 784 Glueer, F., Loew, S., & Manconi, A. (2020, 4). Paraglacial history and structure
785 of the Moosfluh Landslide (1850–2016), Switzerland. *Geomorphology*, 355,
786 106677. Retrieved from [https://www.sciencedirect.com/science/article/
787 pii/S0169555X19300558https://linkinghub.elsevier.com/retrieve/pii/
788 S0169555X19300558](https://www.sciencedirect.com/science/article/pii/S0169555X19300558https://linkinghub.elsevier.com/retrieve/pii/S0169555X19300558) doi: 10.1016/j.geomorph.2019.02.021
- 789 Glueer, F., Loew, S., Manconi, A., & Aaron, J. (2019, 10). From Toppling to Slid-
790 ing: Progressive Evolution of the Moosfluh Landslide, Switzerland. *Journal*

- 791 *of Geophysical Research: Earth Surface*, 124(12), 2899–2919. Retrieved from
 792 <https://onlinelibrary.wiley.com/doi/abs/10.1029/2019JF005019> doi:
 793 10.1029/2019JF005019
- 794 Grämiger, L. M., Moore, J. R., Gischig, V. S., Ivy-Ochs, S., & Loew, S. (2017, 4).
 795 Beyond debuttressing: Mechanics of paraglacial rock slope damage during re-
 796 peat glacial cycles. *Journal of Geophysical Research: Earth Surface*, 122(4),
 797 1004–1036. Retrieved from <http://doi.wiley.com/10.1002/2016JF003967>
 798 doi: 10.1002/2016JF003967
- 799 Grämiger, L. M., Moore, J. R., Gischig, V. S., & Loew, S. (2018, 10). Thermome-
 800chanical Stresses Drive Damage of Alpine Valley Rock Walls During Repeat
 801 Glacial Cycles. *Journal of Geophysical Research: Earth Surface*, 123(10),
 802 2620–2646. Retrieved from <http://doi.wiley.com/10.1029/2018JF004626>
 803 doi: 10.1029/2018JF004626
- 804 Grämiger, L. M., Moore, J. R., Gischig, V. S., Loew, S., Funk, M., & Limpach,
 805 P. (2020, 8). Hydromechanical Rock Slope Damage During Late Pleis-
 806 tocene and Holocene Glacial Cycles in an Alpine Valley. *Journal of*
 807 *Geophysical Research: Earth Surface*, 125(8), 1–24. Retrieved from
 808 <https://onlinelibrary.wiley.com/doi/10.1029/2019JF005494> doi:
 809 10.1029/2019JF005494
- 810 Grillo, B., Braitenberg, C., Nagy, I., Devoti, R., Zuliani, D., & Fabris, P. (2018,
 811 5). Cansiglio Karst Plateau: 10 Years of Geodetic-Hydrological Observa-
 812 tions in Seismically Active Northeast Italy. *Pure and Applied Geophysics*,
 813 175(5), 1765–1781. Retrieved from <http://link.springer.com/10.1007/s00024-018-1860-7>
 814 doi: 10.1007/s00024-018-1860-7
- 815 Gruber, S., & Haeberli, W. (2007, 6). Permafrost in steep bedrock slopes and its
 816 temperature-related destabilization following climate change. *Journal of Geo-*
 817 *physical Research*, 112(F2). Retrieved from [https://agupubs.onlinelibrary](https://agupubs.onlinelibrary.wiley.com/doi/full/10.1029/2006JF000547)
 818 [.wiley.com/doi/full/10.1029/2006JF000547](https://agupubs.onlinelibrary.wiley.com/doi/full/10.1029/2006JF000547)<https://agupubs>
 819 [.onlinelibrary.wiley.com/doi/abs/10.1029/2006JF000547](https://agupubs.onlinelibrary.wiley.com/doi/abs/10.1029/2006JF000547)[https://](https://agupubs.onlinelibrary.wiley.com/doi/10.1029/2006JF000547)
 820 agupubs.onlinelibrary.wiley.com/doi/10.1029/2006JF000547[http://](http://doi.wiley.com/10.1029/2006JF000547)
 821 doi.wiley.com/10.1029/2006JF000547 doi: 10.1029/2006JF000547
- 822 Gualandi, A., & Liu, Z. (2021, 4). Variational Bayesian Independent Component
 823 Analysis for InSAR Displacement Time-Series With Application to Central

- 824 California, USA. *Journal of Geophysical Research: Solid Earth*, 126(4).
 825 Retrieved from [https://agupubs.onlinelibrary.wiley.com/doi/full/](https://agupubs.onlinelibrary.wiley.com/doi/full/10.1029/2020JB020845)
 826 [10.1029/2020JB020845](https://agupubs.onlinelibrary.wiley.com/doi/abs/10.1029/2020JB020845)[https://agupubs.onlinelibrary.wiley.com/](https://agupubs.onlinelibrary.wiley.com/doi/abs/10.1029/2020JB020845)
 827 [doi/10.1029/2020JB020845](https://agupubs.onlinelibrary.wiley.com/doi/abs/10.1029/2020JB020845)[https://onlinelibrary.wiley.com/doi/](https://onlinelibrary.wiley.com/doi/10.1029/2020JB020845)
 828 [doi/10.1029/2020JB020845](https://onlinelibrary.wiley.com/doi/10.1029/2020JB020845)[https://onlinelibrary.wiley.com/doi/](https://onlinelibrary.wiley.com/doi/10.1029/2020JB020845)
 829 [doi: 10.1029/2020JB020845](https://onlinelibrary.wiley.com/doi/10.1029/2020JB020845)
- 830 Gualandi, A., Serpelloni, E., & Belardinelli, M. E. (2016, 4). Blind source separa-
 831 tion problem in GPS time series. *Journal of Geodesy*, 90(4), 323–341. Re-
 832 trieved from <http://link.springer.com/10.1007/s00190-015-0875-4> doi:
 833 [10.1007/s00190-015-0875-4](https://doi.org/10.1007/s00190-015-0875-4)
- 834 Hansmann, J., Loew, S., & Evans, K. F. (2012, 2). Reversible rock-slope de-
 835 formations caused by cyclic water-table fluctuations in mountain slopes of
 836 the Central Alps, Switzerland. *Hydrogeology Journal*, 20(1), 73–91. Re-
 837 trieved from <http://link.springer.com/10.1007/s10040-011-0801-7> doi:
 838 [10.1007/s10040-011-0801-7](https://doi.org/10.1007/s10040-011-0801-7)
- 839 Heki, K. (2001, 7). Seasonal Modulation of Interseismic Strain Buildup in Northeast-
 840 ern Japan Driven by Snow Loads. *Science*, 293(5527), 89–92. Retrieved from
 841 <http://www.sciencemag.org/cgi/doi/10.1126/science.1061056>[https://](http://www.sciencemag.org/cgi/doi/10.1126/science.1061056)
 842 www.sciencemag.org/lookup/doi/10.1126/science.1061056 doi:
 843 [10.1126/science.1061056](https://doi.org/10.1126/science.1061056)
- 844 Hockman, A., & Kessler, D. W. (1950). Thermal and Moisture Expansion Studies of
 845 Some Domestic Granites. *Journal of Research of the National Bureau of Stan-*
 846 *dards*, 44, 395–410.
- 847 Hugentobler, M., Loew, S., Aaron, J., Roques, C., & Oestreicher, N. (2020).
 848 Borehole monitoring of thermo-hydro-mechanical rock slope processes ad-
 849 jacent to an actively retreating glacier. *Geomorphology*, 362, 107190. Re-
 850 trieved from <https://doi.org/10.1016/j.geomorph.2020.107190> doi:
 851 [10.1016/j.geomorph.2020.107190](https://doi.org/10.1016/j.geomorph.2020.107190)
- 852 Jiang, Y., Dixon, T. H., & Wdowinski, S. (2010, 6). Accelerating uplift in the North
 853 Atlantic region as an indicator of ice loss. *Nature Geoscience*, 3(6), 404–407.
 854 Retrieved from <http://www.nature.com/articles/ngeo845> doi: 10.1038/
 855 [ngeo845](https://doi.org/10.1038/ngeo845)

- 856 Leica Geosystems AG. (2013). *Leica MS50/TS50/TM50 User Manual v1.1.1*. Re-
 857 trieved from [http://surveyequipment.com/assets/index/download/id/](http://surveyequipment.com/assets/index/download/id/219/)
 858 [219/](http://surveyequipment.com/assets/index/download/id/219/)
- 859 Leith, K., Moore, J. R., Amann, F., & Loew, S. (2014, 1). Subglacial extensional
 860 fracture development and implications for Alpine Valley evolution. *Journal of*
 861 *Geophysical Research: Earth Surface*, *119*(1), 62–81. Retrieved from [http://](http://doi.wiley.com/10.1002/2012JF002691)
 862 doi.wiley.com/10.1002/2012JF002691 doi: 10.1002/2012JF002691
- 863 Limpach, P., Geiger, A., & Raetzo, H. (2016). GNSS for Deformation and Geohaz-
 864 ard Monitoring in the Swiss Alps. In *Proceedings of the 3rd joint international*
 865 *symposium on deformation monitoring (jisdms 2016), vienna* (pp. 1–4). Vi-
 866 enna.
- 867 Loew, S., Ebnetter, F., Bremen, R., Herfort, M., Lützenkirchen, V., & Matousek, F.
 868 (2007). Annual Opening and Closure of Alpine Valleys. *Felsbau : rock and*
 869 *soil engineering*, *25*(5), 1–60. Retrieved from [https://structurae.net/en/](https://structurae.net/en/literature/journal-article/annual-opening-and-closure-of-alpine-valleys)
 870 [literature/journal-article/annual-opening-and-closure-of-alpine](https://structurae.net/en/literature/journal-article/annual-opening-and-closure-of-alpine-valleys)
 871 [-valleys](https://structurae.net/en/literature/journal-article/annual-opening-and-closure-of-alpine-valleys)
- 872 Loew, S., Grämiger, L., Gischig, V., Glüer, F., & Gschwind, S. (2017). Progres-
 873 sive failure of brittle rock slopes: Field observations, modeling results and
 874 unknowns. In *Progressive rock failure conference, monte verità*. Retrieved from
 875 <https://www.researchgate.net/publication/321220430>
- 876 Ludwigsen, C. A., Khan, S. A., Andersen, O. B., & Marzeion, B. (2020). Vertical
 877 Land Motion From Present-Day Deglaciation in the Wider Arctic. *Geophysical*
 878 *Research Letters*, *47*(19), 1–11. doi: 10.1029/2020GL088144
- 879 Lundberg, A., Ala-Aho, P., Eklo, O., Klöve, B., Kværner, J., & Stumpp, C.
 880 (2016). Snow and frost: implications for spatiotemporal infiltration pat-
 881 terns – a review. *Hydrological Processes*, *30*(8), 1230–1250. Retrieved from
 882 <http://dx.doi.org/10.1002/hyp.10703> doi: 10.1002/hyp.10703
- 883 Marmoni, G. M., Fiorucci, M., Grechi, G., & Martino, S. (2020). Modelling of
 884 thermo-mechanical effects in a rock quarry wall induced by near-surface tem-
 885 perature fluctuations. *International Journal of Rock Mechanics and Mining*
 886 *Sciences*, *134*(May 2019), 104440. Retrieved from [https://doi.org/10.1016/](https://doi.org/10.1016/j.ijrmms.2020.104440)
 887 [j.ijrmms.2020.104440](https://doi.org/10.1016/j.ijrmms.2020.104440) doi: 10.1016/j.ijrmms.2020.104440

- 888 Masset, O., & Loew, S. (2010, 6). Hydraulic conductivity distribution in crys-
889 talline rocks, derived from inflows to tunnels and galleries in the Central
890 Alps, Switzerland. *Hydrogeology Journal*, 18(4), 863–891. Retrieved
891 from <http://link.springer.com/10.1007/s10040-009-0569-1> doi:
892 10.1007/s10040-009-0569-1
- 893 Matsuoka, N. (2008, 7). Frost weathering and rockwall erosion in the southeast-
894 ern Swiss Alps: Long-term (1994–2006) observations. *Geomorphology*, 99(1-4),
895 353–368. Retrieved from [https://linkinghub.elsevier.com/retrieve/pii/](https://linkinghub.elsevier.com/retrieve/pii/S0169555X07005351)
896 [S0169555X07005351](https://linkinghub.elsevier.com/retrieve/pii/S0169555X07005351) doi: 10.1016/j.geomorph.2007.11.013
- 897 McColl, S. T. (2012, 6). Paraglacial rock-slope stability. *Geomorphology*, 153-154,
898 1–16. Retrieved from [https://www.sciencedirect.com/science/article/](https://www.sciencedirect.com/science/article/pii/S0169555X12000979?via%3Dihub)
899 [pii/S0169555X12000979?via%3Dihub](https://www.sciencedirect.com/science/article/pii/S0169555X12000979?via%3Dihub) doi: 10.1016/J.GEOMORPH.2012.02
900 .015
- 901 Mey, J., Scherler, D., Wickert, A. D., Egholm, D. L., Tesauero, M., Schildgen, T. F.,
902 & Strecker, M. R. (2016, 12). Glacial isostatic uplift of the European Alps. *Na-*
903 *ture Communications*, 7(1), 13382. Retrieved from [http://www.nature.com/](http://www.nature.com/articles/ncomms13382)
904 [articles/ncomms13382](http://www.nature.com/articles/ncomms13382) doi: 10.1038/ncomms13382
- 905 Moreira, D. M., Calmant, S., Perosanz, F., Xavier, L., Rotunno Filho, O. C., Seyler,
906 F., & Monteiro, A. C. (2016, 9). Comparisons of observed and modeled elastic
907 responses to hydrological loading in the Amazon basin. *Geophysical Research*
908 *Letters*, 43(18), 9604–9610. Retrieved from [https://agupubs.onlinelibrary](https://agupubs.onlinelibrary.wiley.com/doi/pdf/10.1002/2016GL070265http://doi.wiley.com/10.1002/2016GL070265)
909 [.wiley.com/doi/pdf/10.1002/2016GL070265http://doi.wiley.com/](https://agupubs.onlinelibrary.wiley.com/doi/pdf/10.1002/2016GL070265http://doi.wiley.com/10.1002/2016GL070265)
910 [10.1002/2016GL070265](https://agupubs.onlinelibrary.wiley.com/doi/pdf/10.1002/2016GL070265http://doi.wiley.com/10.1002/2016GL070265) doi: 10.1002/2016GL070265
- 911 Muelchi, R., Rössler, O., Schwanbeck, J., Weingartner, R., & Martius, O. (2021,
912 6). River runoff in Switzerland in a changing climate – runoff regime changes
913 and their time of emergence. *Hydrology and Earth System Sciences*, 25(6),
914 3071–3086. Retrieved from [https://hess.copernicus.org/articles/25/](https://hess.copernicus.org/articles/25/3071/2021/)
915 [3071/2021/](https://hess.copernicus.org/articles/25/3071/2021/) doi: 10.5194/hess-25-3071-2021
- 916 Musso Piantelli, F., Herwegh, M., Anselmetti, F. S., Waldvogel, M., & Gruner,
917 U. (2020). Microfracture propagation in gneiss through frost wedging:
918 insights from an experimental study. *Natural Hazards*, 100(2), 843–860.
919 Retrieved from <https://doi.org/10.1007/s11069-019-03846-3> doi:
920 10.1007/s11069-019-03846-3

- 921 Oestreicher, N. (2018). *Geodetic, hydrologic and seismological signals associated*
 922 *with precipitation and infiltration in the central Southern Alps, New Zealand*
 923 (Doctoral dissertation, Victoria University of Wellington). Retrieved from
 924 <http://researcharchive.vuw.ac.nz/handle/10063/7024>
- 925 Pintori, F., Serpelloni, E., Longuevergne, L., Garcia, A., Faenza, L., D'Alberto,
 926 L., ... Belardinelli, M. E. (2021, 1). Mechanical Response of Shallow
 927 Crust to Groundwater Storage Variations: Inferences from Deformation
 928 and Seismic Observations in the Eastern Southern Alps, Italy. *Journal*
 929 *of Geophysical Research: Solid Earth*, 2020JB020586. Retrieved from
 930 <https://onlinelibrary.wiley.com/doi/10.1029/2020JB020586> doi:
 931 10.1029/2020JB020586
- 932 Prawirodirdjo, L., Ben-Zion, Y., & Bock, Y. (2006, 2). Observation and model-
 933 ing of thermoelastic strain in Southern California Integrated GPS Network
 934 daily position time series. *Journal of Geophysical Research: Solid Earth*,
 935 111(B2). Retrieved from <http://dx.doi.org/10.1029/2005JB003716>[http://](http://doi.wiley.com/10.1029/2005JB003716)
 936 doi.wiley.com/10.1029/2005JB003716 doi: 10.1029/2005JB003716
- 937 Pushpalatha, R., Perrin, C., Le Moine, N., Mathevet, T., & Andréassian, V. (2011,
 938 12). A downward structural sensitivity analysis of hydrological models to
 939 improve low-flow simulation. *Journal of Hydrology*, 411(1-2), 66–76. Re-
 940 trieved from [https://www.sciencedirect.com/science/article/pii/](https://www.sciencedirect.com/science/article/pii/S0022169411006846?via%3Dihub)
 941 [S0022169411006846?via%3Dihub](https://www.sciencedirect.com/science/article/pii/S0022169411006846?via%3Dihub) doi: 10.1016/J.JHYDROL.2011.09.034
- 942 Rango, A., & Martinec, J. (1995). Revisiting the degree-day method for snowmelt
 943 computation. *JAWRA Journal of the American Water Resources Association*.
 944 doi: 10.1111/j.1752-1688.1995.tb03392.x
- 945 Rice, J. R., & Cleary, M. P. (1976). Some basic stress diffusion solutions for fluid-
 946 saturated elastic porous media with compressible constituents. *Reviews of*
 947 *Geophysics*, 14(2), 227. Retrieved from [http://doi.wiley.com/10.1029/](http://doi.wiley.com/10.1029/RG014i002p00227)
 948 [RG014i002p00227](http://doi.wiley.com/10.1029/RG014i002p00227) doi: 10.1029/RG014i002p00227
- 949 Roques, C., Lacroix, S., Leith, K., Longuevergne, L., Leray, S., Jachens, E. R., ...
 950 Selker, J. S. (2021). Geomorphological and geological controls on storage-
 951 discharge functions of Alpine landscapes: evidence from streamflow anal-
 952 ysis in the Swiss Alps and perspectives for the Critical Zone Community.

- 953 *Earth's Future*. Retrieved from [http://www.essoar.org/doi/10.1002/](http://www.essoar.org/doi/10.1002/essoar.10506976.1)
 954 [essoar.10506976.1](http://www.essoar.org/doi/10.1002/essoar.10506976.1) doi: 10.1002/ESSOAR.10506976.1
- 955 Schaltegger, U. (1994). Unravelling the pre-Mesozoic history of Aar and Got-
 956 thard massifs (Central Alps) by isotopic dating : a review. *Schweiz-*
 957 *erische mineralogische und petrographische Mitteilungen*, 74(1), 41–51. doi:
 958 10.5169/seals-56330
- 959 Serpelloni, E., Pintori, F., Gualandi, A., Scoccimarro, E., Cavaliere, A., Anderlini,
 960 L., ... Todesco, M. (2018). Hydrologically Induced Karst Deformation: In-
 961 sights From GPS Measurements in the Adria-Eurasia Plate Boundary Zone.
 962 *Journal of Geophysical Research: Solid Earth*. doi: 10.1002/2017JB015252
- 963 Silverii, F., D'Agostino, N., Borsa, A. A., Calcaterra, S., Gambino, P., Giuliani, R.,
 964 & Mattone, M. (2019). Transient crustal deformation from karst aquifers
 965 hydrology in the Apennines (Italy). *Earth and Planetary Science Letters*, 506,
 966 23–37. Retrieved from <https://doi.org/10.1016/j.epsl.2018.10.019> doi:
 967 10.1016/j.epsl.2018.10.019
- 968 Silverii, F., Montgomery-Brown, E. K., Borsa, A. A., & Barbour, A. J. (2020,
 969 5). Hydrologically Induced Deformation in Long Valley Caldera and Adja-
 970 cent Sierra Nevada. *Journal of Geophysical Research: Solid Earth*, 125(5).
 971 Retrieved from [https://onlinelibrary.wiley.com/doi/abs/10.1029/](https://onlinelibrary.wiley.com/doi/abs/10.1029/2020JB019495)
 972 [2020JB019495](https://onlinelibrary.wiley.com/doi/abs/10.1029/2020JB019495) doi: 10.1029/2020JB019495
- 973 Steck, A. (1983). Geologie Der Aletschregion (Vs). *Bulletin de la Murithienne*, 101,
 974 135–154.
- 975 Sternai, P., Sue, C., Husson, L., Serpelloni, E., Becker, T. W., Willett, S. D., ...
 976 Castelltort, S. (2019, 3). Present-day uplift of the European Alps: Evalu-
 977 ating mechanisms and models of their relative contributions. *Earth-Science*
 978 *Reviews*, 190, 589–604. Retrieved from [https://www.sciencedirect.com/](https://www.sciencedirect.com/science/article/pii/S0012825218304136#f0025)
 979 [science/article/pii/S0012825218304136#f0025](https://www.sciencedirect.com/science/article/pii/S0012825218304136#f0025)<https://linkinghub>
 980 [.elsevier.com/retrieve/pii/S0012825218304136](https://linkinghub.elsevier.com/retrieve/pii/S0012825218304136) doi: 10.1016/
 981 [j.earscirev.2019.01.005](https://linkinghub.elsevier.com/retrieve/pii/S0012825218304136)
- 982 Tsai, V. C. (2011, 4). A model for seasonal changes in GPS positions and seismic
 983 wave speeds due to thermoelastic and hydrologic variations. *Journal of Geo-*
 984 *physical Research*, 116(B4), B04404. Retrieved from [http://doi.wiley.com/](http://doi.wiley.com/10.1029/2010JB008156)
 985 [10.1029/2010JB008156](http://doi.wiley.com/10.1029/2010JB008156) doi: 10.1029/2010JB008156

- 986 Turc, L. (1961). Evaluation des besoins en eau d'irrigation, évapotranspiration po-
 987 tentielle. *Annals of Agronomy*, 12, 13–49. Retrieved from [https://ci.nii.ac](https://ci.nii.ac.jp/naid/20000722287)
 988 [.jp/naid/20000722287](https://ci.nii.ac.jp/naid/20000722287)
- 989 Ustaszewski, M. E., Hampel, A., & Pfiffner, O. A. (2008). Composite faults in the
 990 Swiss Alps formed by the interplay of tectonics, gravitation and postglacial re-
 991 bound: An integrated field and modelling study. *Swiss Journal of Geosciences*,
 992 101(1), 223–235. doi: 10.1007/s00015-008-1249-1
- 993 Valéry, A., Andréassian, V., & Perrin, C. (2014, 9). ‘As simple as possible but
 994 not simpler’: What is useful in a temperature-based snow-accounting rou-
 995 tine? Part 2 – Sensitivity analysis of the Cemaneige snow accounting routine
 996 on 380 catchments. *Journal of Hydrology*, 517, 1176–1187. Retrieved from
 997 <https://linkinghub.elsevier.com/retrieve/pii/S0022169414003321>
 998 doi: 10.1016/j.jhydrol.2014.04.058
- 999 Van Dam, T., Wahr, J., Milly, P. C., Shmakin, A. B., Blewitt, G., Lavallée, D.,
 1000 & Larson, K. M. (2001, 2). Crustal displacements due to continental wa-
 1001 ter loading. *Geophysical Research Letters*, 28(4), 651–654. Retrieved
 1002 from [https://agupubs.onlinelibrary.wiley.com/doi/full/10.1029/](https://agupubs.onlinelibrary.wiley.com/doi/full/10.1029/2000GL012120)
 1003 [https://agupubs.onlinelibrary.wiley.com/doi/abs/](https://agupubs.onlinelibrary.wiley.com/doi/abs/10.1029/2000GL012120)
 1004 [10.1029/2000GL012120](https://agupubs.onlinelibrary.wiley.com/doi/10.1029/2000GL012120)
 1005 doi: 10.1029/2000GL012120
- 1006 Wang, H. F. (2000). *Theory of linear poroelasticity with applications to geomechanics*
 1007 *and hydrogeology*. Princeton University Press. Retrieved from [https://press](https://press.princeton.edu/titles/7006.html)
 1008 [.princeton.edu/titles/7006.html](https://press.princeton.edu/titles/7006.html)
- 1009 Weber, S., Beutel, J., Da Forno, R., Geiger, A., Gruber, S., Gsell, T., ... Yücel,
 1010 M. (2019, 8). A decade of detailed observations (2008–2018) in steep bedrock
 1011 permafrost at the Matterhorn Hörnligrat (Zermatt, CH). *Earth System Science*
 1012 *Data*, 11(3), 1203–1237. Retrieved from [https://essd.copernicus.org/](https://essd.copernicus.org/articles/11/1203/2019/)
 1013 [articles/11/1203/2019/](https://essd.copernicus.org/articles/11/1203/2019/) doi: 10.5194/essd-11-1203-2019
- 1014 Weber, S., Beutel, J., Faillettaz, J., Hasler, A., Krautblatter, M., & Vieli, A.
 1015 (2017, 2). Quantifying irreversible movement in steep, fractured bedrock
 1016 permafrost on Matterhorn (CH). *The Cryosphere*, 11(1), 567–583. Re-
 1017 trieved from <http://www.the-cryosphere.net/11/567/2017/>
 1018 www.the-cryosphere.net/11/567/2017/ doi: 10.5194/tc-11-567-2017

1019 Wegmann, M., & Gudmundsson, G. H. (1999). Thermally induced temporal strain
1020 variations in rock walls observed at subzero temperatures. In K. Hutter,
1021 Y. Wang, & H. Beer (Eds.), *Advances in cold-region thermal engineering and*
1022 *sciences* (pp. 511–518). Berlin, Heidelberg: Springer Berlin Heidelberg.

1023 **7 Supplementary material**

1024 **7.1 Groundwater model**

1025 The lumped rainfall-runoff model GR5J takes as inputs the flow in the river, air
 1026 temperature, total precipitation, and sunshine duration. In the recent past, the average
 1027 flow in spring and summer was higher than during the 20th century, under the influence
 1028 of warming climate, with a higher melting rate of glaciers and earlier snowmelt in spring.
 However, the increase in average river flow is not yet statistically significant. The anal-

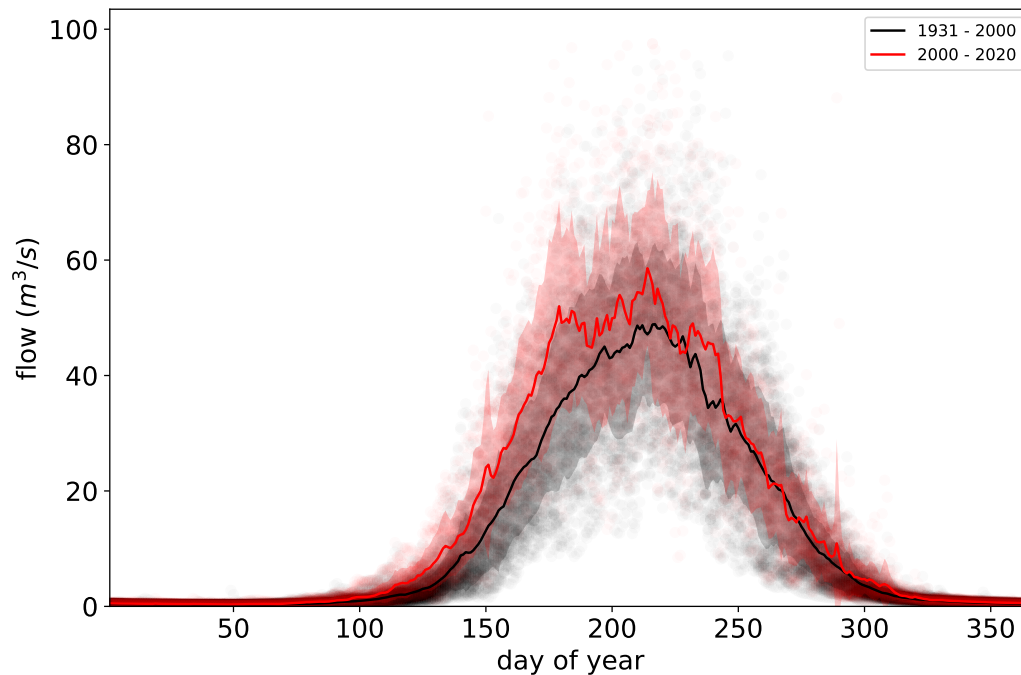


Figure A.1. Daily mean flow in cubic meters per second at the Massa river monitoring station per day of the year. Black dots are daily data points between 1931 and 1999; red dots are data points between 2000 and 2020. Lines are mean per day of the year, and fill is the standard deviation.

1029
 1030 ysis of the frequency content of the river flow dataset (Figure A.2) is performed on the
 1031 data between 1974 and 2020 when the sampling interval was 5 min. A clear annual cyclic-
 1032 ity and semiannual (and less clear terannual) oscillations are visible and can be linked
 1033 to the seasonality in temperature and the impact of snowmelt, glacier melt, and ground-
 1034 water fluctuations. Daily cycles and their multiples are also seen in the time series, and
 1035 correspond to daily fluctuations of glacier melt in summer, with higher flow in the late

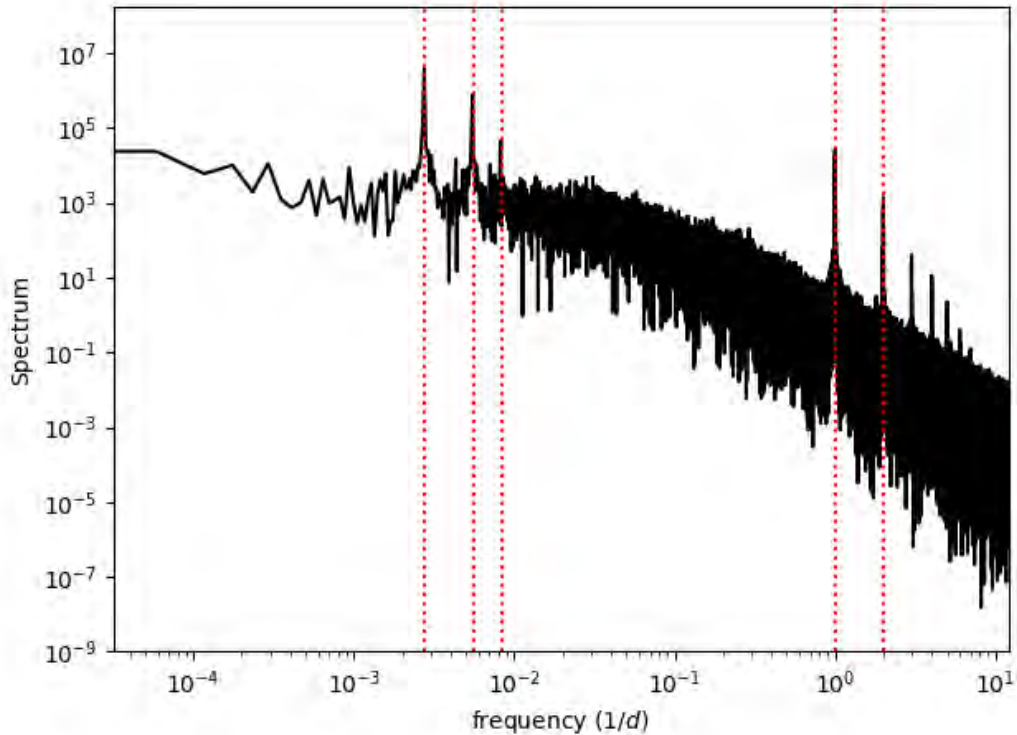


Figure A.2. Periodogram of the hourly measurements of the flow in the Massa River since 1974 (start of sub-daily measurements at the flow gauge). The power spectral density is shown versus frequency in cycles per day with a logarithmic scale. Red dashed lines correspond to cycles with periods of 365 d, 180 d, 120 d, 1 d and 0.5 d.

1036 afternoon and early night and lower flow in the early morning. These daily oscillations
 1037 are not observed during winter. For these reasons, we believe that the contribution of
 1038 the glaciers to the flow in the river is minimal during winter. To minimize the impact
 1039 of the glaciers on the modeled groundwater store, we calibrate the model on periods when
 1040 the average filtered temperature at the Jungfraujoch station drops below -7°C . The cal-
 1041 ibration periods are shown in green in Figure 4.

1042 **7.2 Correlation between deformation and environmental factors**

1043 To help with the interpretation of the datasets and as a tool to determine which
 1044 environmental factors could cause the observed deformation time series, we show the Pear-
 1045 son's correlation coefficients of correlation between time series. In Figure A.4 we show
 1046 the correlation matrix between:

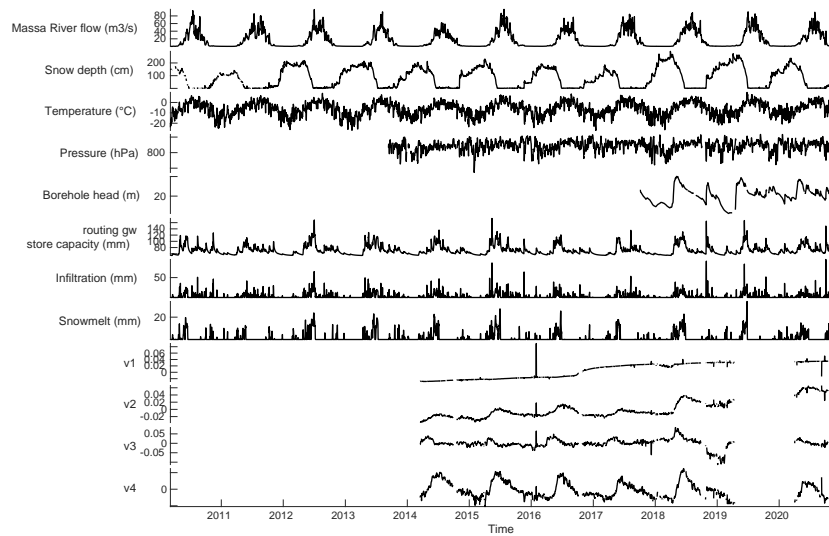


Figure A.3. Dataset used for the correlation matrix, with river flow in the Massa river, snow depth at the Eggishorn station, temperature at the Jungfrauoch station, atmospheric pressure at the Chatzulecher station, observed groundwater head in the borehole B4, modelled groundwater store, infiltration and snowmelt from the GR5J model (Figure 4), as well as the four independent components of the vbICA (Figure 5).

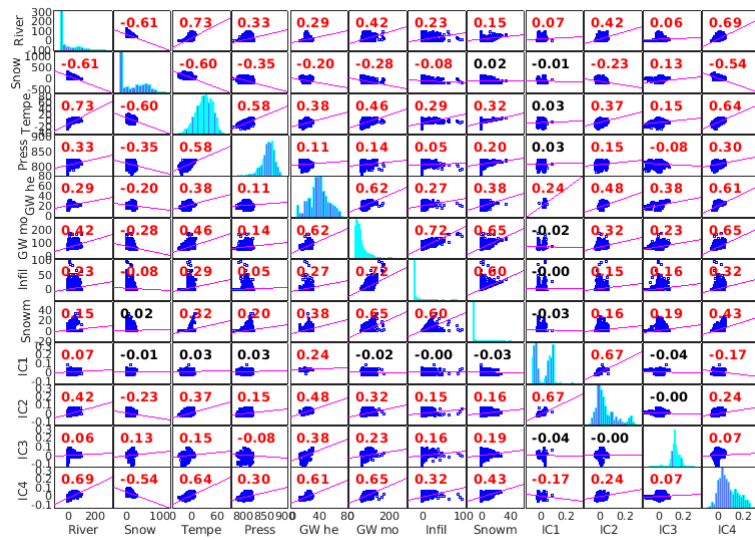


Figure A.4. Correlation matrix (Pearson's correlation coefficients) between the time series from Figure A.4. Histograms of individual inputs are shown on the diagonal.

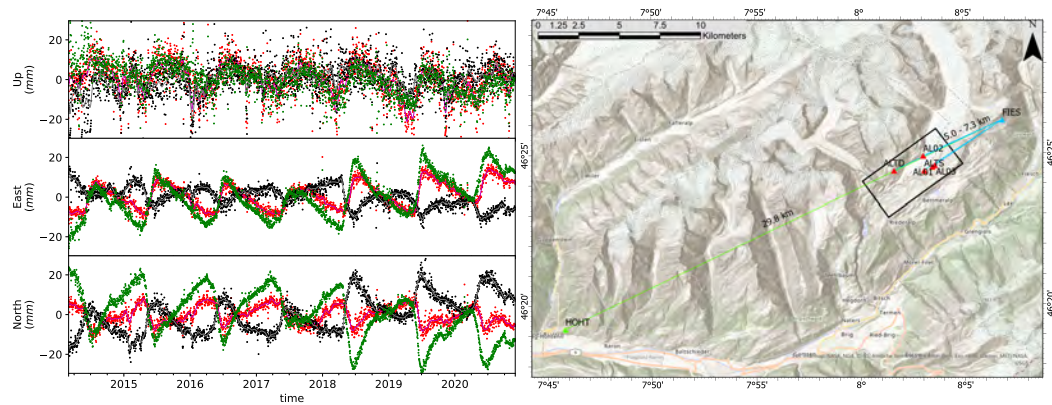


Figure A.5. Three components of displacement of ALTS (black) and FIES (red) cGPS stations relative to HOHT. ALTS relative to FIES (green) represents the baseline between the station, before correction with the displacement of FIES relative to HOHT. The baselines between the single frequency stations used in this study (red triangles) and FIES (blue triangle) as well as the baseline between FIES and HOHT (green triangle) are displayed on a regional map. Black rectangle is the extent of Figure 2.

- 1047
- The water flow in cubic meters per second m^3/s measured at the Massa River flow
- 1048 gauge;
- 1049 • The snow depth in cm measured at the Eggishorn weather station;
 - 1050 • The near-surface air temperature in celsius at the Chatzulecher station;
 - 1051 • The atmospheric pressure in hPa;
 - 1052 • The groundwater store modeled from GR5J in mm;
 - 1053 • The infiltration from snowmelt and rainfall, modeled from GR5J in mm;
 - 1054 • The snowmelt modeled from GR5J in mm;
 - 1055 • The four independent components of deformation identified from the vbICA anal-
 - 1056 ysis.

7.3 Correction of GPS data

1057
1058 The analysis presented in this paper uses HOHT (Hohtenn) as a reference station.
1059 This station (green triangle on Figure A.5), part of the Swisstopo AGNES network of
1060 GNSS stations, is in the Rhone valley, more than 20 km away from our study area. There-
1061 fore, the baseline to this station from the single frequency station installed in the Aletsch
1062 valley would be too long. Instead, we reference the stations used in this study to the FIES
1063 station, at a shorter distance of less than 8 km. The FIES station is itself referenced to
1064 HOHT. For the sake of clarity, we show on Figure A.5 the three components of displace-
1065 ment at the station Fies (relative to HOHT) in red, ALTS (Chatzulecher, relative to FIES)
1066 in green, as well as the resulting correction of ALTS relative to HOHT in black. It is clear
1067 in this Figure that the station FIES is subjected to similar types of motion as the sta-
1068 tions used in this study, but is situated on the opposite side of the mountain range, there-
1069 fore exhibiting a motion in spring to the South-East, similarly to ALTD and AL02.